Development of an ~~image processing~~ automatic thresholding method for wake meandering studies and its application on the data ~~sets~~ set from scanning wind lidar~~and large-eddy simulation~~

Maria Krutova[1], Mostafa Bakhoday-Paskyabi[1], Joachim Reuder[1], and Finn Gunnar Nielsen[1]

[1]Geophysical institute and Bergen Offshore Wind Centre, University of Bergen, Allégaten 70, 5007 Bergen, Norway

Correspondence: Maria Krutova (maria.krutova@uib.no), Mostafa Bakhoday-Paskyabi (mostafa.bakhoday-paskyabi@uib.no)

Abstract.

Wake meandering studies require knowledge of the instantaneous wake ~~shape and its~~ evolution. Scanning lidar data are used to identify the ~~wake pattern~~ wind flow behind offshore wind turbines but do not immediately reveal the wake ~~shape~~edges and centerline. The precise ~~detection of the wake shape and centerline~~ wake identification helps to build models predicting wake behavior. The conventional Gaussian fit methods are reliable in the near-wake area but lose precision with the distance from the rotor and require good data resolution for an accurate fit. The thresholding methods, i.e., selection of a threshold that splits the data into background flow and wake, usually imply a fixed value or manual ~~selection of a threshold~~estimation, which hinders the wake ~~detection~~ identification on a large data set. We propose an automatic thresholding method for the wake shape and centerline detection, which is less dependent on the data resolution and quality and can also be applied to the image data.

We show that the method performs reasonably well on large-eddy simulation data and apply it to the data set containing lidar measurements of the two wakes. Along with the wake ~~detection method~~identification, we use image processing statistics, such as entropy analysis, to filter and classify lidar scans. ~~The image processing method is~~

The automatic thresholding method and the subsequent centerline search algorithm are developed to reduce dependency on the supplementary ~~reference~~ data such as free-flow wind speed and direction. We focus on the technical aspect of the method and show that the ~~centerline found with the image processing is~~ wake shape and centerline found from the thresholded data are in a good agreement with the manually detected centerline and the Gaussian fit method. We also briefly discuss a potential application of the method to separate the near and far wakes and to estimate the wake direction.

1 Introduction

A wake is a complex dynamic structure forming behind a wind turbine due to the kinetic energy extraction from the incoming wind flow. The wake region is characterized by ~~the~~ decreased wind speed and ~~the~~ increased turbulence intensity. The relative velocity deficit~~rapidly decreases to 20% at the downstream distance of five rotor~~diameters ~~(,~~ or wake deficit, is strongest right after the wind turbine. Strongly affected by wind turbine rotor, the region extends up to $4-5$ *D* ~~). Further downstream,~~ rotor diameters depending on the terrain characteristics and stability conditions (Stevens and Meneveau, 2017; Porté-Agel et al., 2020)

. The wake transitions to the far wake, where the recovery to the free flow is considerably slowed down; at the same time, the

25 wake width increases up to ~~3D according to in situ~~ three rotor diameters according to observations (Aitken et al., 2014). The ~~typical~~ turbine spacing in ~~the wind farms is usually 8~~operational wind farms usually reaches $7-10D$ (e.g., London Array), although the optimal spacing is estimated to be even higher in order to reduce the wake effect on downstream turbines (Meyers and Meneveau, 2012; Stevens, 2016). Since the generated wind power is proportional to the cube of the wind speed U^3, the power production gradually decreases if the incoming wind speed drops below the rated wind speed. The increased turbu-

30 lence intensity negatively affects the turbine fatigue loads (Lee et al., 2012). Studying the wake behavior is hence crucial to estimating both the actual power production and the overall lifetime of a wind farm.

Not only the wake expands, but it is also subjected to the wake meandering – oscillations along the rotor axis caused by the movement of large eddies (Larsen et al., 2007, 2008). While the near wake remains primarily stable and follows the wind direction, the far wake oscillates randomly in the horizontal plane with an amplitude exceeding $0.5D$ (Howard et al., 2015; Foti

35 et al., 2016). The far wake also oscillates in the vertical plane, although the velocity fluctuations there are weaker (España et al., 2011). As a result, a downstream turbine is exposed to intermittent flow and, consequently, unequal fatigue loads (Muller et al., 2015; Moens et al., 2019). Additionally, the wake in the Northern hemisphere slightly turns clockwise due to the Coriolis effect (Abkar and Porté-Agel, 2016; van der Laan and Sørensen, 2017) adding more complexity to the wake evolution over time. Knowing only the velocity deficit at a certain downstream distance is insufficient, since the wake meandering strength is char-

40 acterized by the standard deviation of the wake center. Therefore, the wake meandering analysis requires the knowledge of the wake centerline to quantify the instantaneous wake effect on the downwind structures. An appropriate detection method should be able to ~~separate~~ perform wake identification by separating the wake from the free flow and ~~estimate~~ wake characterization by estimating the wake centerline and its statistical characteristics. ~~The method application and their~~ (Quon et al., 2020). Methods' application and capabilities are highly dependent on the input data available.

45 ~~In situ measurements using~~ Measurement campaigns that use scanning lidars provide the most relevant data on the wind flow in a particular wind farm (Trujillo et al., 2010, 2011; Herges et al., 2017). Due to the technical restrictions and ~~costs~~ cost of lidar installation, it is complicated to obtain a three-dimensional scan of the flow around the whole wind farm, although the flow can be reconstructed for a single turbine (Beck and Kühn, 2019). Still, the measurement campaigns span along several months and require data ~~pre-processing~~ preprocessing to sort out invalid measurements. A controlled experiment can be performed on

50 a wind tunnel for model validation or reproduction of specific flow conditions (Snel et al., 2007; Chamorro and Porté-Agel, 2010). The particle image velocimetry (PIV) provides good spatial and temporal resolution of the measured wind field but ~~still~~ deals with the scaled models and has to account for their limitations. A different approach is running a large-eddy simulation (LES) of a wind turbine or a wind farm. While LES provides a wide range of possibilities to simulate atmospheric conditions and wind farm configuration, its representation of a wake strongly depends on the implemented turbulence closure (Moriarty

55 et al., 2014; Mehta et al., 2014; Martínez-Tossas et al., 2018) and wind turbine model (Porté-Agel et al., 2011; Martínez-Tossas et al., 2015). A relatively new development is quantitative study of wind farm wakes from the satellite data (Ahsbahs et al., 2020). The satellites generally have a lower spatial resolution than scanning lidars and measure wind speed on the horizontal near-surface plane but still provide general information on the flow around wind farms.

Several wake ~~detection~~ identification methods exist, varying in ~~the~~ complexity and input data requirements (Quon et al., 2020). Among the variety of ~~wake detection~~ the methods, we focus on the thresholding and Gaussian fitting because they are applicable to a 2D lidar scan in a horizontal or inclined plane. The most common wake ~~detection method is fitting a~~ identification method is to fit a one- or two-dimensional Gaussian distribution to the velocity deficit across the wake at various downstream positions and get estimations of the wake center and width from the fitted function (Fleming et al., 2014; Vollmer et al., 2016; Krishnamurthy et al., 2017). The method can be applied both to the averaged and instantaneous wake, although the irregular wake shape of the latter complicates the detection. For better accuracy, the fitting requires wind speed data in a fine spatial resolution. A sufficient spatial resolution is achieved by large-eddy simulation or particle image velocimetry. The Gaussian fit method can ~~be also~~ also be applied to the scanning wind lidar data, provided the wake region is resolved well enough. Overall, the fitting method efficiency depends on the data quality and spatial resolution. The method also requires the free-flow wind speed to calculate the wake deficit.

Alternatively, a threshold value can be defined~~to~~. In the simplest case, the threshold splits the range of available values into two: all values below the threshold fall into one group, while the remaining values form the second group. When applied to the wind field for the wake identification, the threshold would split the data into the wake and free-flow points. Thresholding methods depend less on the data resolution and mainly rely on the wind speed values. The simplest thresholding method ~~defines~~ sets a threshold based on the wind speed ratio in the wake and the free flow. ~~The detection is applied up to a~~ As shown by España et al. (2011), the method is effective for a regular flows, e.g., in a wind turbine: a threshold of 95% of the free-flow wind speed identified the continuous part of the wake up to the downstream distance of $6-8D$~~distance downstream the turbine, where the wake structure remains primarily continuous. The post-processing may require filtering and smoothing to decrease the noise (España et al., 2011).~~ . The resulting shape required smoothing and filtering to reduce the noise. Bastine et al. (2015) used a stricter threshold of 40% of the maximum wake deficit on the LES data to extract the wake core and perform proper orthogonal decomposition on the processed wind field.

~~A fixed threshold value~~ The thresholding method is not widely used due to its restriction: it applies an empirical coefficient that does not account for ~~wind speed distribution and data quality~~ the data quality and wind speed fluctuations in the flow field, which may be a common issue for a lidar scan. ~~The fitting methods also depend on the data quality and spatial resolution and may require additional data such as wind direction. We, therefore, refer to image processing techniques that depend less on the data availability and can be applied both to the image or processed wind speed data.~~ We propose an ~~image processing method with an~~ automated threshold estimation, previously developed for the whitecaps detection – Adaptive Thresholding Segmentation method (ATS) (Bakhoday-Paskyabi et al., 2016). We adapt the method for the wake ~~applications~~ identification and develop new routines to estimate the wake centerline without a priori knowledge of the wind direction.

This study focuses on the technical aspect of the ATS method and discusses its advantages and limitations. The method is applied to ~~the~~ a scanning lidar data set containing wakes from two wind turbines and various wake-wake ~~or wake-turbine~~ interactions. The ~~measurement site and lidar~~ measurements and LES setup are described in Sect. ~~2.1, and the data preprocessing is reviewed~~ 2. Lidar data required additional preprocessing, described in Sect. ~~2~~3. In the same section, we preview diagnostic techniques ~~using~~ by using image entropy to evaluate and classify the data. ~~In addition to the lidar data, we also describe wake~~

~~detection based on LES data as a proof of concept.~~ The application of the image processing method to the wake ~~and centerline~~
95 ~~detection~~ identification and characterization is detailed in Sect. 4. We demonstrate our algorithm on the idealized LES data as a proof of concept in Sect. 5. We then apply the ~~image processing techniques~~ same algorithm to the lidar data and compare the result with the manual wake detection, deficit-based thresholding and the Gaussian fit method in Sect. 6. The findings are summarized in Sect. 7. In the Appendix, we briefly discuss the differences between wake ~~detection~~ identification from the lidar scan data and the respective grayscale image.

2 ~~Site~~ Data description~~and measurement setup~~

2.1 Lidar and reference data

~~In this study, we use radial wind speed data recorded with a scanning Doppler wind lidar Leosphere WindCube 100S~~ We use measurements of wind speed and wind direction recorded during the Offshore Boundary-Layer Experiment at FINO1 (OBLEX-F1) campaign. The FINO1 platform is located in the North Sea at 54° 00' 53.5" N 6° 35' 15.5" E, 45 km to the north
105 of the German island of Borkum. The ~~installed lidar is oriented towards the *alpha ventus* wind farm.~~

~~The~~ *alpha ventus* wind farm is located in the vicinity of FINO1 and consists of 12 wind turbines arranged in a rectangular pattern (Fig. 1). The wind turbines AV1−AV6 are of the type Repower 5M with a hub height of 92 m and a rotor diameter of 126 m; AV7−AV12 are of the type AREVA M5000 with a hub height of 91.5 m and a rotor diameter D of 116 m. The row and column distances between the turbines vary within 800−850 m, approximately seven rotor diameters, $7D$. The distance
110 between FINO1 and the closest wind turbine, AV4, is 405 m.

The FINO1 meteorological mast has a cup anemometer installed at 90 m above sea level and a vane installed at 100 m above sea level. The wind speed and direction measured with those instruments are used to characterize the free flow. We will further refer to them as the reference wind speed and direction, respectively.

The scanning Doppler wind lidar Leosphere WindCube 100S installed at FINO1 is oriented towards the *alpha ventus* wind
115 farm. The closest scanned wind turbine, AV7, is located at 919 m or 7.92D from FINO1 ~~.~~

~~A schematic shows (a) the location of FINO1 platform, map made with Natural Earth, (b) wind farms and platforms near FINO1, status in 2015-2016, and (c) *alpha ventus* wind farm layout, maximum lidar scan area and scanning height at the position of each wind turbine.~~

(Fig. 1c). The lidar is installed at 23.5 m above sea level and operates in a Plan Position Indicator (PPI) scanning mode. In
120 this mode, the azimuth of the lidar beam changes between 131.5° and 179.5° at an elevation angle of 4.62°. The lidar scans the south-western sector of the *alpha ventus* wind farm and captures wake patterns from two wind turbines, AV7 and AV10. The third wind turbine, AV11, stays outside of the lidar range in most scans, but a part of its wake is visible for the specific wind directions. The wind turbine AV7 is scanned near the hub height at approximately 97 m. The farther wind turbines AV10 and AV11 are scanned above the top of the blade tip at 158 m and 188 m, respectively.
125 ~~In addition to the lidar data, we use the wind speed and wind direction time series from the FINO1 meteorological mast as a reference. The wind speed and direction are measured at and , respectively.~~
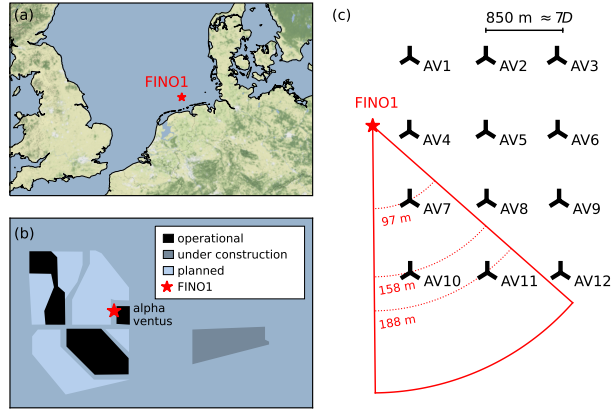
Figure 1. A schematic shows (a) the location of FINO1 platform, map made with Natural Earth, (b) wind farms and platforms near FINO1, status in 2015-2016, and (c) *alpha ventus* wind farm layout, maximum lidar scan area and scanning height at the position of each wind turbine.

3 ~~Data description~~

2.1 ~~Lidar measurements at~~ *~~alpha ventus~~*

The lidar measurements partially cover the day of September 24, 2016 and capture a variety of wake-wake interactions. The ~~data set used in this study contains the first of each hour. The~~ consecutive lidar scans are separated by approximately 45 s – the time required for the lidar to finish one scan. ~~Overall, the~~ The data set contains 600 lidar scans, which are split into 24 subsets of 25 scans~~each~~. Each subset contains the first $20-22$ minutes of each hour. For the simplicity of presentation and referring, we number the lidar scans from 1 to ~~600 (Table 1).~~ 600.

The ~~image processing~~ ATS algorithm accepts the input data as a grayscale image. The wind speed data ~~is adjusted~~ of each lidar scan are normalized by scaling to the range of [0, 1] to imitate the grayscale intensity as

$$I = \frac{U_{\max} - U}{U_{\max} - U_{\min}}, \tag{1}$$

where U is the wind speed ~~value~~ measured at a point, $U_{\min}$ and $U_{\max}$ are minimum and maximum wind ~~speed~~ speeds registered in a particular lidar scan. For the lowest wind speed $U = U_{\min}$ (potential wake points), $I = 1$ denotes the points with the highest intensity. Similarly, the highest wind speed for $U = U_{\max}$ (free-flow points), $I = 0$ indicates the points with the lowest intensity. ~~Figure 2 presents an example lidar scan plotted in polar coordinates and then transformed into Cartesian coordinates~~

The wake identification is performed on the data stored in a polar coordinate matrix (Fig. 2a). For a better presentation, the resulting data are plotted in the Cartesian coordinates as a scanned sector (Fig. 2b).
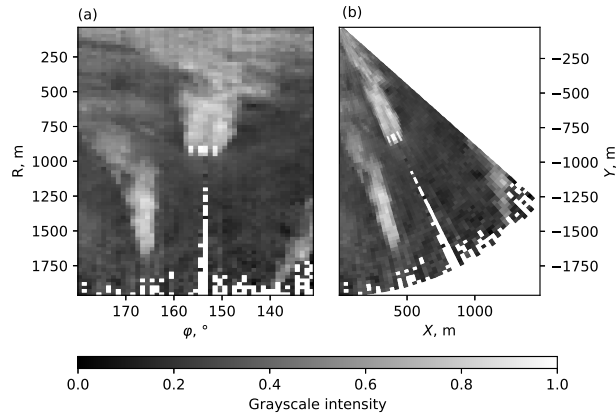
Figure 2. An example lidar scan #497 taken on September 24th 2016 19:18:20 UTC+0 at reference wind speed $7.4\,\mathrm{ms}^{-1}$ and reference wind direction $151.14°$. The original data are presented in (a) the polar coordinates R, φ as stored in the matrix and (b) the Cartesian coordinates X, Y.

~~An example lidar scan #221 taken on September 24th 2016 08:17 UTC+1 at reference wind speed and reference wind direction 171.2. The original data is stored in (a) the polar coordinates R, φ and converted to (b) the Cartesian coordinates X, Y.~~

2.1 Large-eddy simulation

~~The wake detection is performed on the data stored in the polar coordinates. The resulting data are converted to the Cartesian coordinates for a better presentation~~ We also perform a large-eddy simulation to demonstrate and verify the performance of the ATS method and compare it against the Gaussian wake identification and characterization method described further in Sect. 4.3. We use the PALM LES code with a built-in actuator disc with rotation (ADR) wind turbine model (Maronga et al., 2020). The results produced with the model were shown to capture the reduction of the wake deficit with the downstream distance at the rate similar to the encountered for wind turbines (Vollmer et al., 2015, 2017; Doubrawa et al., 2020). The wake recovery aspect is particularly important to test the ATS method performance in the far wake. The currently used polynomial kernel also allows fitting the Gaussian function to compare it with the ATS method.

The domain contains $2304 \times 576 \times 192$ points and has the horizontal grid spacing of $4\,\mathrm{m}$. The vertical spacing below $600\,\mathrm{m}$ is also $4\,\mathrm{m}$. Above $600\,\mathrm{m}$, the vertical spacing is stretched with a factor of 1.08, capped at maximum $8\,\mathrm{m}$ grid cell height. The roughness length of $z_0 = 0.0005\,\mathrm{m}$ corresponds to the calm sea surface. The Coriolis forcing is enabled for the latitutde of $54°$, and the wind speed components are set to $u = 10.5\,\mathrm{ms}^{-1}$ and $v = -2.6\,\mathrm{m}^{-1}$ so that the flow rotation is compensated and the flow is aligned with the x-axis resulting in the horizontal speed of $10\,\mathrm{ms}^{-1}$ at the hub height. The surface temperature is $277\,\mathrm{K}$ and increases by $1\,\mathrm{K}$ per $100\,\mathrm{m}$. Neither heat flux nor surface heating are activated. During the simulation the turbulence intensity reaches 6.6%.

6

The reference NREL 5MW wind turbine has a hub height of 102 m and a diameter of $D_r = 126$ m and is placed in the center of the domain so that the wake length can reach up to $20D_r$.

165   The LES is used solely to generate idealized wake data. No direct comparison to the lidar data is performed.

3 Lidar data pre-processing and classification

3.1 Data quality

Working with the current data set, we encountered two types of noise affecting the quality of the wake identification through thresholding: small wind speed fluctuations not directly caused by the wake and high

170   wind speed values appearing due to a measurement error.

The measurement errors are primarily caused by the difference between wind direction and lidar orientation. The lidar measures radial velocity, which can be represented through three directional wind speed components u, v, and w, and the information on the line of sight of the lidar beam, given by the azimuth ϕ and elevation angle θ:

$$U = u\sin\phi\cos\theta + v\cos\phi\cos\theta + w\sin\theta \tag{2}$$

175   When the wind blows along the lidar's line of sight, the measured radial velocity is essentially the horizontal wind speed. With the wind direction differing from the line of sight, the radial velocity deviates from the actual wind speed magnitude. In the case of crosswind – the wind direction is close to perpendicular to the line of sight – the radial velocity tends to zero and does not represent the actual wind speed. The measurements taken during the crosswind event are more prone to errors compared to other wind directions.

180   When plotted against the reference wind direction, the reference wind speed and mean radial wind speed of a lidar scan show strong discrepancy for a range of wind directions (Fig. 3). With the lidar scanning in the range of $131.5-179.5°$, the crosswind effects can be expected for the wind directions of $221.5-269.5°$. As shown in Fig. 3, the crosswind effects already appear for the wind direction above $210°$. The scans taken near crosswind direction show a large number of non-physical wind speed values reaching $100-1000\,\mathrm{ms}^{-1}$. We refer further to these scans as 'corrupted'.

185   Occasionally, we also observe weaker spikes in the radial wind speed, most of which are localized at the position of a wind turbine AV10, implying a measurement error due to the lidar beam reflection from rotating blades. The reference and mean radial wind speeds remain in the good agreement for the wind directions below $210°$ despite containing spikes in the wind speed data. Nevertheless, the outliers cause an intensity skew when the wind speed data are normalized to the range of [0, 1] (Fig. 4). The intensity distribution peak moves to the right, with the left side containing occasional

190   low bumps caused by the spikes (Fig. 4d).

In the example, the middle scan (Fig. 4b) has a wind speed spike of $15\,\mathrm{ms}^{-1}$, while the reference wind speed reaches $5.8\,\mathrm{ms}^{-1}$. The radial wind speed magnitude measured in the spike region stays below $7\,\mathrm{ms}^{-1}$. The lidar scan after normalization is less contrast compared to the adjacent lidar scans.
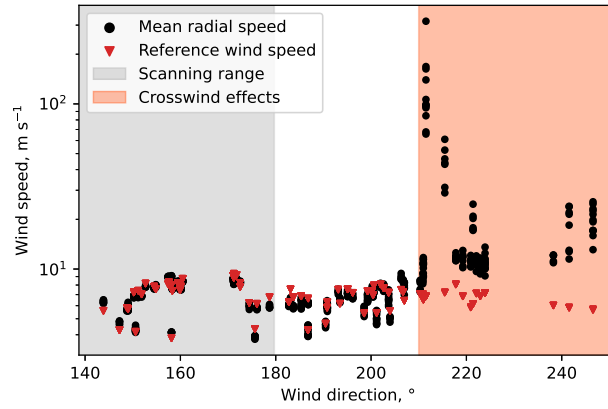
7

Figure 3. Comparison of the mean radial wind speed and the reference wind direction in the data set.
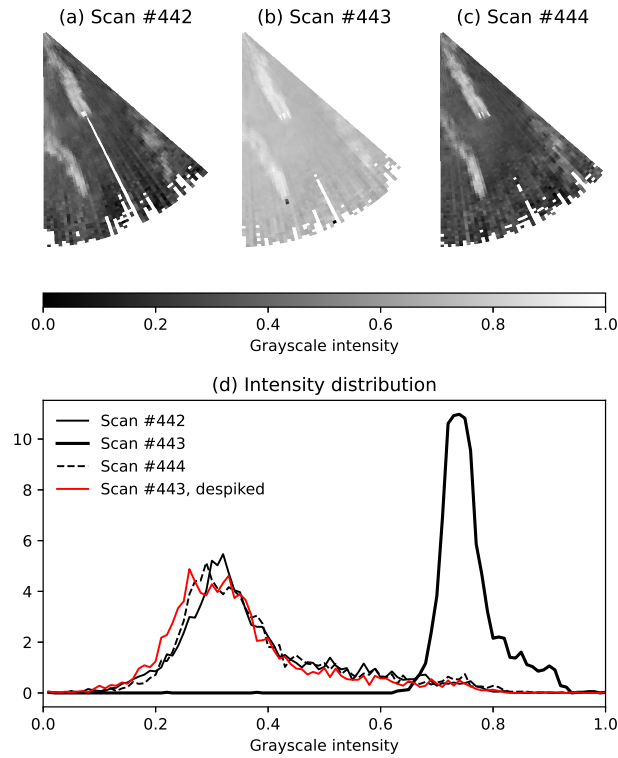

Figure 4. Consecutive lidar scans from the bimodal subset. ~~Scans (a)~~ No outliers are present in scans #442 and ~~(c) have a valid wind speed range~~#444, while scan ~~(b)~~ #443 has wind speed spikes near the wind turbine position and in the far range; subplot (d) shows the intensity distribution for the same scans.

To preserve the uniformity between consequent lidar scans of the same subset, we perform despiking – detection and removal
of the spikes. The spikes are detected based on the wind speed value and the difference with the adjacent points. We delete all
values higher than $30\,\mathrm{ms}^{-1}$ and check the remaining data for the local maximums. ~~We consider a wind speed of~~ An empirically
chosen wind speed difference of $7\,\mathrm{ms}^{-1}$ proved to be enough to designate a local maximum as a spike. When a spike consists
of a single or double point, it is replaced by a NaN value and the resulting gap is filled by interpolation to retain the continuous
wind field. ~~Larger clusters of high wind speed values are considered noise~~ Three or more adjacent points designated as spike
are considered a noise cluster; in such cases, gap filling after removal is not performed.

Since the lidar is oriented towards the closest wind turbine, a string of missing values – a wind turbine 'shadow' – is always
present in the lidar scans regardless of the wind direction. The shadow rarely crosses wind turbine wakes and ~~did~~ does not
noticeably affect the performance of the wake detection methods. Hence we do not perform a gap filling to remove the shadow
in addition to the despiking.

3.2 Information entropy and data classification

We introduce entropy criteria as an alternative to using reference ~~data~~ wind speed and direction for quality control. The entropy
application ranges from finding a threshold (Pun, 1981) to object classification in an image (e.g., satellite map segmentation
by Long and Singh (2013)). Here, we calculate it primarily for the diagnostic purposes and data classification into subsets.

The information entropy is a measure of noise in the data. It can be calculated for the whole data set as well as across the
rows or columns of a rectangular matrix containing 2D data. We apply Shannon entropy S (Shannon, 1948) as follows:

$$S = -\sum_{i=1}^{n} P(x_i) log_2 P(x_i), \tag{3}$$

where $P(x_i)$ is the probability density function (PDF) of the variable x_i (here – intensity) to occur in the data. If the entropy
tends to zero, it indicates uniform data. ~~High~~ A high entropy value implies disturbances in the lidar scan due to wakes or noise.
~~However, too strong disturbances caused by measurement errors are reflected as entropy decrease due to the approach we use.~~
~~As shown earlier, the outliers cause intensity skew after normalization to the range of 0, 1(Fig. 4b). With the maximum values of~~
~~, the intensity skew after normalization becomes even stronger. The valid wind speed measurements become indistinguishable~~
~~and the lidar scan in question is perceived to be uniform, hence its entropy is lower than for the scans containing mostly valid~~
~~measurements.~~

~~For the directional entropy, we select either~~

To analyze lidar scan features, we calculate entropy for the partial data instead of the whole scan. We select wind speed
values ~~across the beam range or across the azimuth~~ either in the radial or azimuthal direction and calculate a PDF ~~for~~ of this
sample to pass it to the entropy function. An example ~~directional entropy~~ is presented in Fig. 5. The top and the left parts of
the example scan in polar coordinates do not contain wakes, hence the entropy calculated for the respective rows and columns
is lower than for the wake regions. The entropy calculated ~~across the azimuth~~ in the radial direction (Fig. 5a) is higher for
columns ~~containing~~ crossing both wakes instead of one due to higher disturbance rate. An additional entropy increase near the
azimuth of $130-140°$ can be explained by high noise at the lidar scan border. The entropy calculated ~~across the beam range~~ in

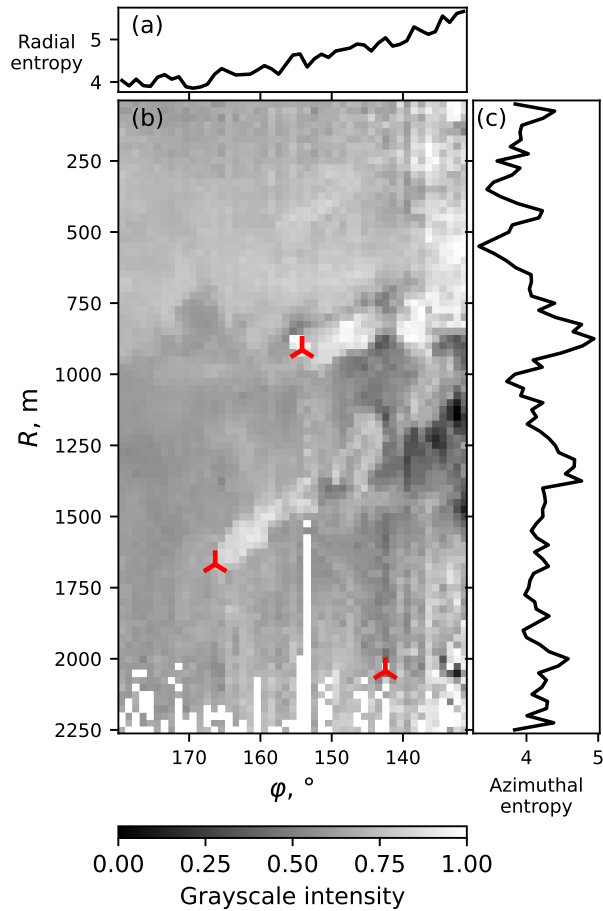**Figure 5.** The entropy calculated in the (a) radial and (c) azimuthal directions of (b) the lidar scan #61. Reference wind speed is $7.19\,\mathrm{ms^{-1}}$ and reference wind direction is $203.68°$

the azimuthal direction (Fig. 5c) ~~has a prominent~~ shows a peak for the AV7 wake. The AV10 ~~wake produces two less prominent peaks indicating thinner~~ far wake produces less prominent peak indicating a wake spread along longer distance ~~. We can utilize changes in the entropy to detect common features in the lidar scans~~ and not aligned with the azimuthal direction.

230   We calculate the entropy ~~across the azimuth and beam range~~ in radial and azimuthal directions for all lidar scans before preprocessing~~and combine them~~. Combined into two plots, the entropies present an overview of the data set (Fig. 6). The respective wind turbine positions are marked on the right axis. The lower color bar limit is adjusted for ~~better presentation, while the actual entropy values reach zero for certain lidar scans~~the better presentation of the features contained in non-corrupted scans. For the scans with low noise, the entropy values fall into the range of $4-5$ both in the azimuthal and radial direction.

235 The entropy calculated ~~across the beam range~~ in the azimuthal direction highlights several lidar scans with a ~~significant entropy decrease compared to other cases~~substantial entropy decrease (Fig. 6a) ~~. Those~~ — the value drops below two and tend to zero.
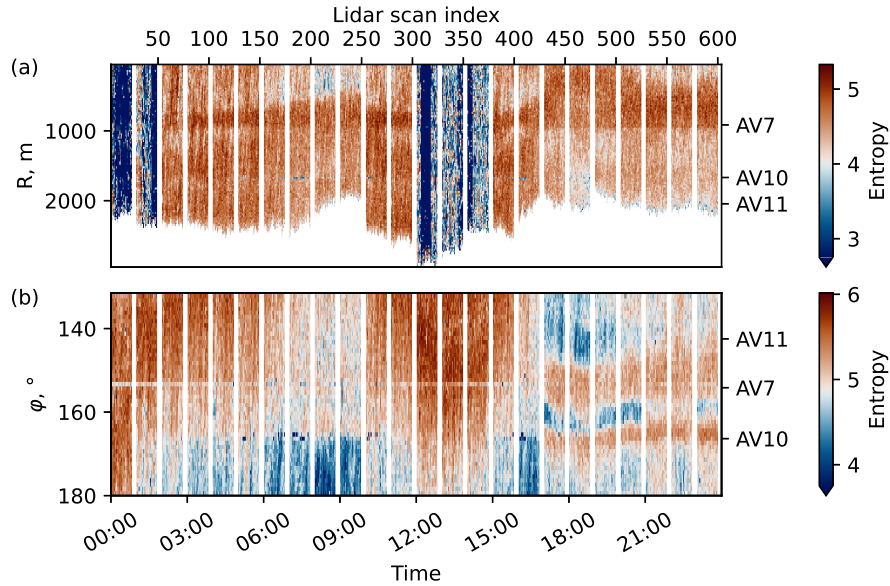
10

Figure 6. ~~The directional entropy calculated across~~ Entropy of the raw lidar data, all 600 lidar scans combined: (a) ~~azimuth φ and (c) beam range R of~~ azimuthal entropy, (b) ~~the lidar scan #61.~~ radial entropy.

The same scans are also characterized by the measurements corrupted due to the crosswind effect. The spiked data ~~also leads to entropy decrease although not as gradual. The corresponding scans can be~~ in non-corrupted scans leads to a local entropy decrease, seen as occasional ~~vertical stripes in (Fig. 6), e.g. , series of scans after~~ blue dots mostly at the location of AV10.

240 Series of such points can be seen for scans #~~400.~~ 176-200 and #401-410.

~~The remaining subsets have a~~ Non-corrupted subsets show similar entropy distribution ~~across the beam range~~ in the azimuthal direction (Fig. 6a). A wake from the wind turbine AV7 can be seen as an increase of entropy near the turbine's ~~position~~ location. A weaker increase of entropy can be also seen for AV10, for example, in scans #51−175.

The entropy calculated ~~across the azimuth~~ in the radial direction is distributed uniformly for the corrupted subsets (Fig. 6b)~~also~~

245 ~~shows consistent features for the corrupted lidar scans: the subset containing scans #1− 25 and #301− 350 shows a substantial decrease of entropy. Among the remaining scans , ,~~ but otherwise does not have as strong difference to non-corrupted data, as the entropy in the azimuthal direction (Fig. 6a). Part of non-corrupted scans (#51−300 and #376−425) show a gradient-like pattern caused by the absence of wakes in 170−180° sector (low entropy) and wakes and border noise in 130−140° sector (high entropy). The pattern is weaker for scans #176−250, where the border noise is absent and wakes are aligned along the

250 line connecting wind turbines, thus disturbing a smaller area of a lidar scan. The scans #426−600 combined demonstrate a horizontal stripe pattern, caused by the wind blowing towards the lidar~~and wakes forming in the near scanning range. The entropy increase matches~~. Wakes forming across the scanned azimuths cause the entropy increase in the radial direction matching the positions of AV7 and AV10, as marked ~~in~~ on the graphs.
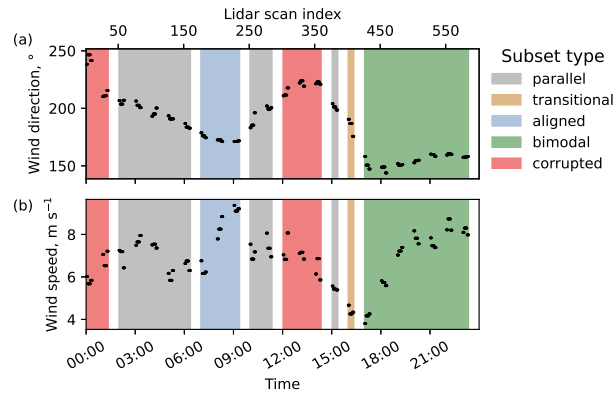
Figure 7. Classification of the subsets and overview of the reference wind direction (a), and wind speed (b).

~~Directional entropy of the raw lidar data, all 600 lidar scans combined: (a) entropy calculated across the beam range R, and~~
255 ~~(b) entropy calculated across the azimuth φ.~~

The low entropy ~~criteria agree~~ criterion agrees well with the crosswind ~~criteria~~ criterion on which scans are likely to contain a high amount of corrupted data. In general, the scans with a high ~~data~~ corruption rate can be ~~easily~~ identified based on the percentage of the data points exceeding a specific wind speed limit. ~~The total~~ Since the reference wind speed does not exceed $10\,\text{ms}^{-1}$, we consider the wind speeds above $30\,\text{ms}^{-1}$ to be a likely measurement error. The corrupted scans consistently
260 have at least 1% of points exceeding this limit. The percentage drops to $0-0.05\%$ for the rest scans and corresponds to the occasional spikes.

The number of corrupted scans is ~~five subsets, each containing 25 scans~~ 125, i.e., about 1/5 of the total number of scans. Classification of the remaining valid scans requires either ~~prior~~ a priori knowledge of the reference wind direction (which may be unavailable if we work with ~~the~~ image data) or visual evaluation of the wake features (which may be complicated for a large
265 data set). Entropy criteria can ~~potentially~~ simplify the classification by presenting a condensed overview of the data set. Using the entropy and intensity histograms, we classify the subsets into the following groups:

1. **Parallel wakes subset**, Fig. 8a: The wakes do not interact with each other. Some noise may occur at the lidar scan's border due to the wind direction approaching the value where the crosswind effects start. Since the wakes propagate towards this border and add to the disturbance, the entropy calculated in the radial direction shows a consistent increase
270 near the azimuth of $131°$. The entropy calculated in the azimuthal direction shows a strong increase near the location of AV7 due to the wake and a weaker disturbance caused by AV10. The intensity histogram of an averaged subset tends to be more symmetrical than in other subsets and has a peak close to the intensity of 0.5. The intensity histogram of a single scan has a peak deviating from the center depending on the amount of noise. Parallel wakes are the most common case for this data set.
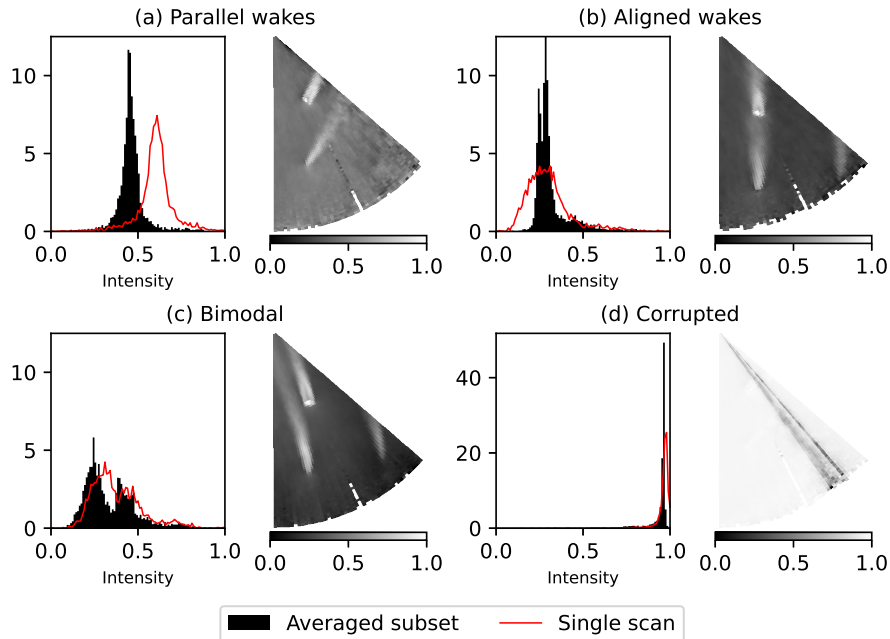
12

Figure 8. Sample averaged subsets and intensity histograms corresponding to the averaged subset and a single scan within the subset. The wind speed data are normalized to imitate the grayscale intensity. Despiking and removal of non-physical wind speeds are not performed to preserve the characteristics before preprocessing.

2. **Aligned wakes subset**, Fig. 8b: The wind blows along the line connecting wind turbines AV7 and AV10 so that the former is subjected to a wake. The entropy patterns are generally similar to the parallel wakes subset, except that a footprint of the AV10 wake is no longer visible for the entropy calculated in the azimuthal direction. The wind direction is closer to the scanned azimuths range and measurements have less noise compared to the parallel subset, hence the scans show slightly lower entropy. Compared to the parallel wakes subset, the histogram peak is shifted to the left. The histogram peak may split into two small peaks located close to each other when the wakes are not perfectly aligned.

3. **Transitional subset**. The wind direction changes, so both parallel and aligned wakes can be observed in the subset. This behavior is observed for a single subset containing scans #401 − 425. The transition to slightly lower entropy can be seen for the entropy calculated in the radial direction at azimuths 130-150° (Fig. 6b).

4. **Bimodal subset**, Fig. 8c: The wind blows along the lidar beam. Two long wakes are formed behind the wind turbines and merge in the lidar near range. Since the near range is scanned at a high resolution (Fig. 2), the far wake is represented by a larger percentage of points compared to the other subsets. Consequently, the intensity histogram approaches a bimodal distribution, which is especially prominent for the averaged subset. The larger peak represents the free flow, while the

smaller peak corresponds to the far wakes of AV7 and AV10. The two peaks may merge resulting in one flat peak. The scans have little noise; the increase of entropy, especially in the radial direction, highlights the presence of the wakes.

290   5. **Corrupted subset**, Fig. 8d: The lidar scan is characterized by the amount of non-physical measurements (wind speed higher than $30\,\mathrm{m/s}$) exceeding 1% of the lidar scan points. While the valid measurements still take the largest share of a single scan, they are now considered 'low' wind speeds in a comparison to the maximum value. Due to the normalization (Eq. 1) that converts low values into light pixels, the histogram tends to the far right side, forming a sharp peak in intensity values between 0.9 and 1.0. The entropy in the azimuthal direction is lower than in other subsets and approaches zero,

295   while the entropy in the radial direction tends to be more uniform than in non-corrupted scans and does not react to the presence of a wake.

The overview of the subsets and reference values is presented in Fig. 7 and Table 1 containing wind speed, wind direction and entropy averaged over each subset. A sample histogram averaged for a typical subset from each group is shown in Fig. 8 together with a single scan histogram from the same subset.

300   Classification of the subsets and overview of the reference wind direction (a), and wind speed (b).

Sample averaged subsets and corresponding intensity histograms. The wind speed data are normalized to imitate the grayscale intensity.

3.3 LES setup

We have also performed a large-eddy simulation to verify the performance of the image processing algorithm and compare

305   it against the Gaussian method described further in Sect. 4.3. For that purpose, we use the PALM LES code with a built-in actuator disc with rotation (ADR)wind turbine model (Maronga et al., 2020). The results produced with the model were shown to reproduce the wake shape rather accurately (Vollmer et al., 2015). Particularly, the model resolves the double peak in the wake deficit distribution near the rotor.

The domain contains $2304\times 576\times 192$ points and has the horizontal grid spacing of . The vertical spacing below is also ,

310   above the vertical spacing is stretched with a factor of 1.08, capped at maximum grid cell height. The reference NREL 5MW wind turbine has a hub height of and a diameter of $D_r =$ and is placed in the center of the domain so that the wakelength can reach up to $20D_r$. The surface temperature is and increases by per . Neither heat flux nor surface heating are activated. During the simulation the turbulence intensity reaches 6.6%.

The LES is used solely to generate idealized wake data. No direct comparison to the lidar datais performed.

Table 1. Overview of the lidar data subsets.

Data type	Subset	Scans	WSPD, m s^{-1}	WDIR, °	Entropy	% of data
Parallel wakes	3	51−75	6.99	205.3	5.11	
	4	76−100	7.71	202.7	5.29	
	5	101−125	7.48	196.0	5.38	
	6	126−150	6.05	191.4	5.35	
	7	151−175	6.58	184.0	5.01	33.3
	11	251−275	7.10	187.8	5.12	
	12	276−300	7.41	200.2	5.37	
	16	376−400	5.45	200.9	5.02	
Transitional	17	401−425	4.38	184.5	4.76	4.2
Aligned wakes	8	176−200	6.32	176.2	4.69	
	9	201−225	8.30	172.2	5.28	12.5
	10	226−250	9.19	171.3	5.30	
Bimodal	17	426−450	4.11	151.5	5.44	
	18	451−475	5.71	147.3	5.31	
	19	476−500	7.22	150.9	5.72	
	20	501−525	7.83	154.2	5.67	29.2
	21	526−550	7.52	159.4	5.64	
	22	551−575	8.46	160.1	5.72	
	23	576−600	8.16	157.7	5.70	
Corrupted	1	1−25	5.80	243.3	1.54	
	2	26−50	6.85	212.1	2.31	
	13	301−325	7.27	213.4	1.53	20.8
	14	326−350	7.06	222.2	2.64	
	15	351−375	6.41	222.0	2.52	

315 4 Methodology

Wake detection includes two stages (Quon et al. (2020)): wake identification – a separation of the wake from the free flow, and wake characterization – further analysis of the identified wake. We focus on the wake identification methods, particularly, an identification method using thresholding and also provide an algorithm for the wake characterization through centerline detection from the thresholded data.
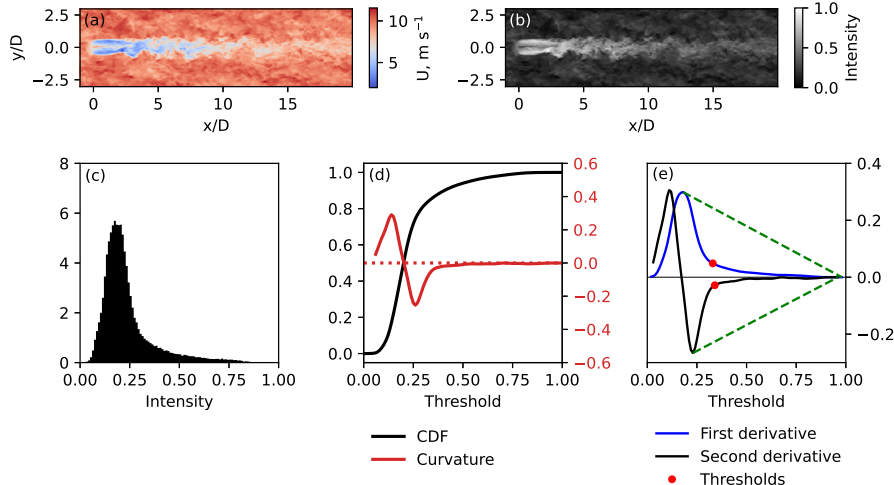
Figure 9. Sample LES wake and threshold detection. (a) Original instantaneous flow; (b) same flow normalized to the range of [0, 1]; (c) the intensity histogram of the normalized data; (d) CDF of the normalized data and CDF plot curvature; and (e) first and second derivatives of the CDF and the estimated thresholds.

4.1 ~~Automatic~~ Wake identification using automatic threshold detection

The ~~automatic thresholding methods aim to~~ thresholding methods split an image into background (in our case – free flow) and foreground (wake). Despite lidar data having ~~large~~ a considerable amount of disturbances in the free flow, the wind speed distribution in a ~~single~~ lidar scan tends to have one peak~~.~~, either sharp or flattened (Fig. 8). The wake points take a small share of the lidar scan stored in polar coordinate matrix, while the remaining points belong to the free-flow – i.e., the most prominent peak contains free-flow points. The exception is the bimodal subset, where the far wakes characterized by high number of points (Fig. 2). As the result, the histogram of a scan from the bimodal subset may have two peaks depending on the intensity of the far wakes. To make our wake identification method universal, we build it upon threshold detection from a single histogram peak. The specifics of the wake identification in the bimodal case are further described in Section 6.4 and in the Appendix.

A single peak limits the applicability of the common thresholding methods that search for the local minimum of a bimodal histogram (Otsu, 1979). The lidar scan structure has similarities with ~~the~~ ocean surface images: a background with small disturbances and bright whitecaps. Bakhoday-Paskyabi et al. (2016) described three methods of ~~the~~ an automated threshold detection for the whitecaps. We choose an Adaptive Thresholding Segmentation (ATS) method identified to be fast and reliable by the original study. The basic principles of the ATS method are introduced here on a test example of an ~~averaged~~ instantaneous LES wake.

Figures 9a and 9b show the wind speed field of ~~a 10-minute averaged~~ an instantaneous LES wake and the same data normalized to the range of [0, 1]. A threshold T is ~~a~~ an intensity value in the range [0, 1] that separates ~~the~~ free flow and

16

wake points. After the threshold is applied to the normalized wind field, a binary matrix WP is constructed from I as follows:

$$WP(i,j) = \begin{cases} 0: & I(i,j) \leq T - \text{free-flow point,} \\ 1: & I(i,j) > T - \text{wake point.} \end{cases} \tag{4}$$

The intensity threshold can be converted back to the ~~wind speed~~ radial velocity threshold U_{th} by ~~:~~ reverting the normalization expression Eq. 1 as

$$U_{th} = U_{\max}(1-T) + U_{\min}T. \tag{5}$$

The normalized wind speed data ~~can be~~ are represented as an intensity histogram (Fig. 9c). Let $H(x)$ for $x \in [0,1]$ be the cumulative distribution function (CDF) of the intensity data. Then $H'(x)$ and $H''(x)$ are its first and second derivatives, respectively. With respect to the definition of intensity I in Eq. (1), the wake points are located in the histogram's tail, while the free-flow points form a peak on the left side. The transition region where the peak tends to the tail is a good choice to ~~look for a~~ search for a suitable threshold. We detect the threshold at the point where the CDF slope is close to constant, i.e., the curvature $C(x)$ approaches zero.

$$C(x) = H''(x)[1 + H'(x)^2]^{-3/2}. \tag{6}$$

The curvature graph tail (Fig. 9d) may fluctuate and complicate the detection of the zero curvature. Instead, we look at the first and second derivatives $H'(x)$ and $H''(x)$ separately. The threshold value T_2 is selected as an inflection point at the right side of the second derivative graph (Fig. 9e). A similar point in the first derivative graph ~~can be~~ T_1 is used as a ~~complementary value~~ ~~to improve accuracy.~~ control value. We select the threshold as an average value between first and second derivative inflection points to smooth the threshold detection outcome. If the points initially laid close to each other, the averaged threshold $T = (T_1 + T_2)/2$ would not deviate too far from T_2. If the difference between T_1 and T_2 is high, the smoothing prevents the threshold from being too strict and leaving weak wakes undetected.

In the case of the lidar data, the derivative plots ~~may~~ have strong oscillations. Therefore, we fit a polynomial function on the range between intensity I_k, corresponding to the most prominent local extremum and maximum intensity $I_{max} = 1$. We fit a ~~polynomial function with the order of five~~ function $F(k) = a_1 + a_2/k^5$, since the corresponding fit returned low root-mean-square error (RMSE) while not altering the inflection point location significantly.

~~The estimated inflection points should lie close to each other. We select the threshold as an average value between first and second derivative inflection points to smooth the detection outcome. Alternatively, for example in the case of a smooth one-peak histogram, only a second derivative inflection point can be used.~~

After the threshold is found, we apply it to the data as described in Eq. (4) and obtain a binary matrix WP that represents thresholded data. Each matrix point corresponds to an image pixel. Because of the wake irregularity, especially in the lidar scan, the method usually detects several clusters of high-intensity points. Any cluster may be a part of a wake as well as falsely detected noise. We do not yet distinguish between wake and noise and refer to all detected clusters as 'wake shapes'. Due to the code implementation, the ~~centerline can be also estimated without the prior knowledge of wind direction.~~ detected points

---

Procedure 1 Automatic threshold detection

Input: $U(r,\phi)$ {raw lidar data}

  despike $U(r,\phi)$

Input: $k \in [0,1]$ step 0.01

  $I \leftarrow (U_{max} - U)/(U_{max} - U_{min})$

  $H \leftarrow f(I,k)$ {get the intensity histogram}

  $H_1 \leftarrow \partial H/\partial k$

  smooth H_1 with moving average $n = 4$

  $H_2 \leftarrow \partial^2 H/\partial k^2$

  smooth H_2 with moving average $n = 4$

  normalize H_1 and H_2

  $P_1 \leftarrow$ fit $F(k) = a_1 + a_2/k^5$ on $[k(\max H_1), 1]$

  $P_2 \leftarrow$ fit $F(k) = a_1 + a_2/k^5$ on $[k(\min H_2), 1]$

  $T_1 \leftarrow P_1$ inflection

  $T_2 \leftarrow P_2$ inflection

Output: $T \leftarrow (T_1 + T_2)/2$

  Sample LES wake and threshold detection. (a) Original flow averaged over 10 minutes; (b) same flow normalized to the range of 0, 1; (c) the intensity histogram of the normalized data; (d) CDF of the normalized data and CDF curvature; and (e) first and second derivatives of the CDF and the estimated thresholds.

  {threshold data as $WP(r,\phi)$ }

4.2 ~~Wake detection using image processing techniques~~

~~In the thresholded image, it can be expected that the near wake will be the largest continuous structure of all detected shapes due to the highest wake deficit. The presumed wake shape is also most likely to contain a wind turbine within it. Points identified as a wake can be extracted for further analysis, either as a shape or a borderline contour. The wake centerline is then defined as a middle line of the wake shape. To fully automate the centerline detection, we require the wind turbine coordinates, and preferably, the wind direction. The wind direction is particularly useful to distinguish wake shapes from noise, as it allows to exclude shapes detected in the upwind direction as false positives. Nevertheless,~~

if $I(r,\phi) < T$ **then**

  $WP(r,\phi) \leftarrow 0$ {free-flow point}

else

  $WP(r,\phi) \leftarrow 1$ {wake point}

end if

---

belong to the same shape as long as the constituting points are adjacent in the matrix WP. The shapes touching only by the

370 corners are considered to be separate shapes.

~~We demonstrate the centerline detection on a simple case of 10-minute averaged LES wake (Fig. 12a). After the threshold is applied, the wake is presented as a continuous structure (Fig. 12b). In the example, the wake expansion is not detected for $x/D > 10$ due to the wind speed recovery to the free flow near $y/D \approx 2$. Nevertheless,~~

4.2 Wake characterization from the data thresholded by the ATS method

375 For the wake characterization, we detect the centerline of a wake shape. The centerline search method starts with extracting a contour of a wake shape; the further algorithm is based upon the geometrical properties. It should be noted that the centerline search algorithm does not strictly depend on the ATS method and can be used as a stand-alone algorithm that requires thresholded data as an input.

To start the centerline search method, we require a procedure to determine which shapes were correctly identified as a wake.
380 The ATS method searches for the ~~detected shape is suitable for the centerline detection.~~ high-intensity points corresponding to the highest wake deficit. Containing the highest wind speed decrease, the near-wake region perfectly satisfies this condition. Therefore, it can be expected that the near wake will be one of the largest continuous shapes among the detected and will contain a wind turbine within or near it. The borderline contour of such shape is extracted for further analysis. The wake centerline is then defined as a centerline of the extracted contour.

385 Assuming the outline of the shape as wake boundaries, we estimate the wake centerline using the following algorithm:

1. ~~We start~~ The algorithm starts by drawing a circle of radius $1D$ around the wind turbine and ~~mark~~ marks points where the circle crosses the borders of the wake shape. If the circle ~~happens~~ appears to lie within the wake shape completely, the initial radius ~~should be increased~~ is increased until intersections are found.

2. The midpoint of the arc inside the wake ~~presumably~~ contour indicates the wake direction and is stored as the centerline
390 midpoint.

3. ~~We increase the circle diameter and repeat~~ The circle diameter is increased by a pre-defined step, e.g., $0.1D$, and the steps $1-2$ are repeated until the end of the wake shape is reached~~(Fig. 12c)~~.

~~Wake and centerline detection for a sample 10-minute averaged LES wake: (a) normalized flow field, same as Fig. 9b; (b) wake shape after threshold is applied; and (c) shape contour and centerline detection.~~

395 ~~In an irregular wake shape~~ This short algorithm works as it is for an ideal case of a smooth wake contour and known wind direction matching the wake direction. However, the circular lines may cross the ~~wake boundaries~~ irregular wake contour several times. ~~For the initial step, it may be difficult to resolve the ambiguity, if the wind direction is unknown.~~ Considering the near wake to be wide and continuous, we ~~assign the midpoint of the longest arc inside~~ expect the centerline point to lie within the wake shape~~as the centerline point~~. We also assume that the wake does not turn gradually further downstream. Therefore,
400 the segment between the last known and unknown midpoint should turn by a relatively small angle compared to the previous

19

segment. The ~~new midpoint also has to lie within the wake shape~~wind or wake direction is advantageous to distinguish wake shapes from noise, as it allows narrowing the search by disregarding shapes detected in the upwind direction as false detection.

The currently used centerline search algorithm 2 provided further includes these and several other rules for selection of a
405   wake point when an ambiguity is present. Fig. 10 shows an example of resolved ambiguity based on the wind direction. If the wind direction was not available, an estimated wake direction could be used instead with the same outcome.

Procedure 2 Wake centerline detection

$N(r,\phi) \leftarrow$ label $WP(r,\phi)$ {enumerate detected shapes}

Input: (x_w, y_w) or (r_w, ϕ_w) {wind turbine coordinates}

  if $WP(r_w, \phi_w) = 1$ **then**

    $n \leftarrow WP(r_w, \phi_w)$ {select a wake shape containing the wind turbine}

  else

    find $n \in N$ and R {select the largest detected shape near the wind turbine location}

  end if

  $L \leftarrow$ boundary contour of the wake shape n

  for $d = 1$ to $15D$ step $0.1D$ **do**

    $C \leftarrow$ contour of a circle with radius r centered at (x_w, y_w)

    $p^i \leftarrow$ intersect L and C

    calculate midpoints on the arc between (p^i, p^{i-1})

    $N_p \leftarrow$ number of midpoints inside the wake shape n

    if $N_p == 0$ **then**

      $(x_c^r, y_c^r) \leftarrow$ NaN {the circle does not cross the wake contour}

    else if $N_p == 1$ **then**

      $(x_c^r, y_c^r) \leftarrow$ midpoint p_1, p_2 {centerline point is the only midpoint inside a wake}

    else

      {ambiguous centerline point, limit the search}

      $\alpha \leftarrow$ deviation from the know wind or wake direction for each valid midpoint

      $(x_c^r, y_c^r) \leftarrow \min(\alpha^{(x_c^r, y_c^r)})$

    end if

  end for

Output: X_c, Y_c

Generally, this centerline-search method does not require a priori knowledge of the wind direction. However, it may be difficult to resolve the ambiguity on the first step, if the wind direction is unknown. For example, the aligned wakes subset (Fig. 8b) and, to a certain extent, also the bimodal subset (Fig. 8c) introduce ambiguity in a wake direction for the downstream
410   wind turbine AV7. ~~The~~ A circle drawn around AV7 may cross the detected wake in at least four points. The algorithm will
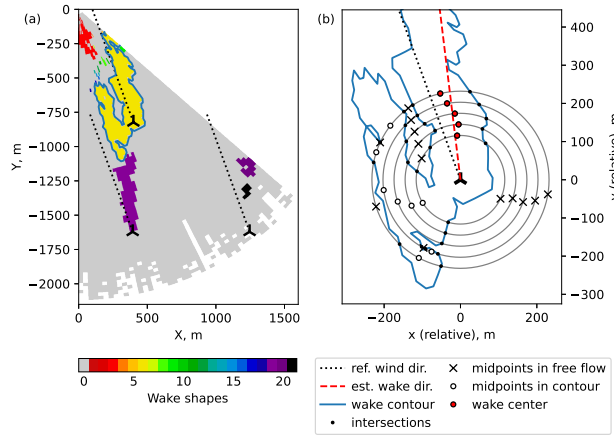
Figure 10. An example wake centerline detection in an ambiguous case.

in turn identify downstream and upstream points as potential centerline points. To continue the search, the algorithm has to select only one direction. In the absence of the reference wind direction, the ~~either by applying the reference wind direction or starting the detection from the upstream wind turbine~~ ambiguity can be resolved AV10.

~~The estimated centerline is further used to calculate the~~ by approximating the wake direction first.

415   The procedure to approximate the wake direction runs similarly to the centerline search, with few alterations. First, the step is increased, but the algorithm is run for a shorter length until $4D$ downstream, so only the most well resolved part is processed. All midpoints laying inside the wake contour are accepted, since there is yet no way to make a distinction between them. A linear function $y(x) = ax$ is then fit to the identified midpoints. If the coefficient of determination is negative ($R^2 < 0$), the fit is too inaccurate, and the procedure is repeated for another wind turbine. ~~The wake from~~

420   The intercept value a of the best fit is the ~~wind turbine AV11 is usually weak and easily confused with the noise; we do not consider this wake in our analysis~~ arctangent of the mathematical wind direction (Fig. 11). The approximated meteorological wind direction is then

$$\Phi_{MET} = \frac{3}{2}\pi - \Phi_{MATH} = \frac{3}{2}\pi - \arctan a \tag{7}$$

The approximated wake direction may strongly deviate from the actual wake direction, so it is only used to resolve ambiguity.
425   The actual wind direction is estimated from the full centerline. We convert the coordinates of the centerline points for the AV7 and AV10 wakes to the Cartesian system and subtract the respective wind turbine positions to get a set of the relative centerline coordinates. We assume a centered data set and add a point (0, 0) corresponding to the relative wind turbine position. The wake from the wind turbine AV11 is prominent only for the bimodal subset and is too short and easily confused with the noise in the other subsets. We do not consider this wake in our analysis due to the little information it can provide compared to the other two wakes. The composed data set is fitted with the linear regression, and the fitted line indicates the estimated wake direction.
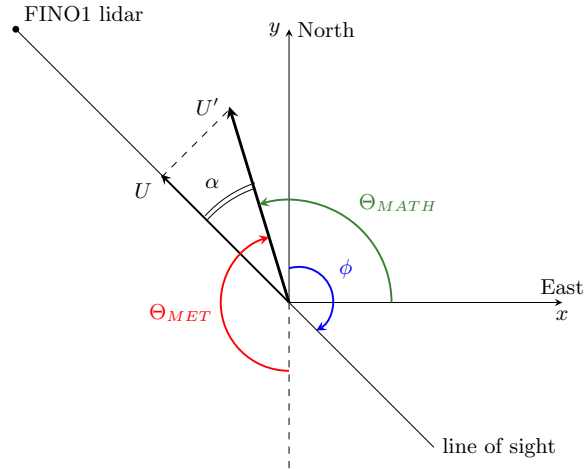
Figure 11. The relation between radial wind speed U, actual wind speed U', azimuth angle ϕ and meteorological and mathematical wind directions Θ_{MET} and Θ_{MATH}.

4.3 Wake ~~detection~~ identification and characterization using the Gaussian method

The wake deficit distribution is similar to the Gaussian distribution in the far wake (Ainslie, 1988) and often shows a double Gaussian peak in the near wake (Magnusson, 1999). ~~This feature~~ The similarity to the Gaussian distribution makes a base for a widely used method to detect wake boundaries and centerline (Vollmer et al., 2016; Krishnamurthy et al., 2017). The method requires the data in a two-dimensional horizontal plane, which makes it versatile and practical to use for the wake ~~detection. A small plane inclination can be allowed as long as the wake profile is not subjected to the wind shear effects.~~ identification and characterization.

~~A normalized~~ Due to the lidar elevation angle, AV10 is scanned near the top tip and does not show a double wake. The scan resolution near AV7 is not always sufficient to resolve a pronounced double wake. Therefore, we fit the wake deficit distribution ~~is fitted with the~~ with a single Gaussian function:

$$F(y) = A \exp\left(-\frac{(y-\mu)^2}{2\sigma^2}\right), \tag{8}$$

where the amplitude A, mean value μ, and standard deviation σ are the parameters to fit; the variable y is a coordinate ~~across the rotor axis~~ on a line perpendicular to the wind direction. The fitting starts from $1D$ to avoid uncertainties caused by a weak double wake observed for AV7. We attempt fitting for the wake deficit profiles up to $15D$ downstream distance covering the length of most wakes in the lidar data set.

For a wake deficit distribution, the fitted ~~single~~ Gaussian function $F(y)$ reaches its maximum at $y = \mu$, i.e., the estimated mean μ gives the wake center position ~~across the rotor axis~~. The wake boundaries are defined through the mean value μ and the

standard deviation σ as $\mu \pm 2\ln 2\sigma$ so that the velocity deficit at the wake boundaries is 5% of the velocity deficit at the wake center (Aitken et al., 2014).

450 ~~Unlike the centerline detection using image processing, the Gaussian method should be applied to the data extracted along the straight-line. We attempt fitting for the wake deficit distributions up to 15D downstream distance covering the length of most wakes~~ The Gaussian function is fitted to the wake deficit of $\Delta U(y) = 1 - U/U_0$, thus a knowledge of the free-flow wind speed U_0 is also required. Since the background flow is rather non-uniform in the lidar ~~data set~~scans, we probe the velocity at each cross-section at $1.6D$ from the rotor axis (Krishnamurthy et al., 2017). The LES data use the wind speed at the hub height
455 as the free-flow wind speed.

We run the Gaussian ~~fit~~method in an automatic mode. The ~~wake deficit distribution is extracted for a straight line~~ method should be applied to the data extracted along the straight-line perpendicular to a pre-defined search direction~~, usually the reference wind direction. The Gaussian fit~~. The algorithm thus requires knowledge of the wind direction before the fitting. The algorithm is also dependent on the accuracy of the wind direction measurements and the similarity between reference
460 wind and actual wake direction. During our analysis, we observed an offset of about 5° between the directions, which caused fitting errors for otherwise clear wake. To reduce the influence of a possible discrepancy between wind and wake direction, we recalculate the search direction ~~after enough points are accumulated. For example, the fitting starts from at 0.5D with a step of 0.1~~every five points by fitting the linear function to the previously found center points.

The wake deficit profiles extracted for fitting have a width of $2.5D$~~along the search direction. After the wake deficit at 2~~,
465 except for the bimodal subset. There, the profile width is decreased to $1.75D$ ~~is fitted, we fit the linear regression to~~ after reaching the downstream distance of $6D$. The correction is active only for the ~~previously found center points and recalculate the search direction. The process is then repeated for each step along the wake.~~

~~It should be noted that a wake usually expands beyond rotor diameter size. Hence, it is important to have more data points in the wake deficit distribution to improve fitting results. At the same time, the extracted line should not be too long to exclude~~
470 ~~disturbance from the other wakes, if present, or low wind-speed streaks~~scans after #500 where the AV10 far wake and the AV7 wake come close enough, but do not yet merge completely and allow separation. If the Gaussian function is fit to a wider profile there, the fitting would mistake higher deficit in the AV7 near wake for the center of the AV10 wake. Reducing the extracted wake profile width improves the centerline detection in the AV10 far wake and delays the first occurrence of this error, although does not always prevent it.

475 **4.4** ~~Wake deficit threshold~~**Deficit-based wake identification**

In addition to the Gaussian fit, we apply a threshold based on the wake deficit ~~criteria~~criterion. The method assumes that ~~the~~a point belongs to the wake if the wind speed ~~at it~~there is less or equal to 95% of the free-flow wind speed (España et al., 2011)~~. Here we assign~~; here – the reference wind speed.

The lidar measures radial velocity U (Eq. (2)). If the wind direction differs from the scanned azimuths, the reference wind
480 speed ~~as the free flow speed.~~measured by a cup anemometer noticeably deviates from the free-flow radial velocity. Normally, a lidar retrieval procedure should be performed to reconstruct the actual wind field. Since we are only interested in the wind speed

23

values, but not the local flow direction, we apply a simple expression to re-project the radial velocity and take the magnitude of the calculated wind speed.

$$U'_{r,\phi} = \frac{U_{r,\phi}}{\cos\alpha} \tag{9}$$

where $U_{r,\phi}$ is the measured radial velocity at the beam range r and azimuth ϕ; $U'_{r,\phi}$ is the estimated magnitude of the real velocity, and α is the angle between the radial and actual wind speed vectors (Fig. 11). Equation (9) assumes that the flow moves in the reference wind direction at each scanned point regardless of the wake influence and other flow disturbances.

The angle α is calculated as the difference between reference wind direction Θ_{MET}, given according to the meteorological convention, and the azimuth ϕ (Fig. 11). I.e., Eq. (9) changes to

$$U'_{r,\phi} = \frac{U_{r,\phi}}{\cos\alpha} = \frac{U_{r,\phi}}{\cos(\Theta_{MET} - \phi)} \tag{10}$$

4.5 ~~Manual wake detection~~

Since the normalization (Eq. (1)) is not performed, the deficit-based method does not necessarily require despiking – all high-value outliers would be assigned to the background flow by the threshold condition. However, the method requires additional information on the free-flow, such as the wind speed and direction, to perform the simple retrieval.

~~To evaluate the performance of the ATS method, we~~ The threshold is applied to the wind speed field recalculated with Eq. (10) instead of the original radial velocity field used for the ATS method. Therefore the direct comparison of the thresholds is complicated. Instead, we compare the thresholded images and evaluate the detection accuracy against the manual wake identification.

4.5 Manual wake identification and characterization

We perform a manual segmentation to select an optimal threshold for each lidar scan and use it as a ~~reference.~~ 'true' identification. The manual threshold is defined in a way to represent the minimum threshold required to identify a wake shape suitable for the automatic centerline detection as described in Sect. 4.2. The comparison against manual wake identification then would show, whether the ATS method is capable to automatize the threshold selection and improve its flexibility compared to the deficit-based thresholding.

Since the available scans represent different wake-wake ~~and wake-turbine~~ interactions, the criteria for a reasonable threshold ~~varies~~ vary over the subsets. In order to reduce human error, we use the following qualitative criteria:

1. The shape of the wake should be distinguishable well enough not to be ~~mistaken with~~ misinterpreted as noise.

2. The noise should be reduced near wind turbines AV7 and AV10 but is allowed near AV11 since its wake has low importance in this study.

3. The ~~shapes of~~ identified wakes from AV7 and AV10 should not merge to ease the centerline detection.

We also perform a manual centerline detection. A ~~presumed~~ centerline is drawn over the lidar scan as a line or series of points. For further comparison with ~~wake detection~~ other wake characterization methods, it is converted to the Cartesian coordinates using a plot digitizer. Unlike the manual ~~detection of the wake shape~~threshold detection, the manual ~~centerline detection~~ wake characterization is more prone to errors, especially in the far-wake region, where the wake becomes less distinguishable from the free flow. Due to ambiguity and complexity of the manual centerline detection, we select only few lidar scans to demonstrate the methods' performance in the parallel, aligned and bimodal subset.

5 ~~Results~~

For brevity, the wake identification and characterization methods are further referred to as listed in Table 2.

~~In this section, we first present a proof of concept ATS detection on less noisy LES data and compare it to the Gaussian method. For the lidar data, we perform an extensive comparison to the manual wake detection and evaluate the accuracy of the ATS method.We further compare the performance of the ATS and Gaussian methods and discuss the application~~

Table 2. Summary of the wake detection methods

Name	Main characteristics
Manual	**Input data**: Radial velocity field. **Identification**: Threshold value based on the visual evaluation. **Characterization**: Digitized centerline drawn over the lidar scan. **Automation**: No. **Flexibility**: Yes.
Deficit-based	**Input data**: Retrieved velocity field, Eq. (9), reference wind speed. **Identification**: Threshold value based on the wake deficit compared to the free flow. **Characterization**: Not performed. **Automation**: Yes. **Flexibility**: No.
Gaussian	**Input data**: Radial velocity field, wind direction, wind turbine locations. **Identification**: Gaussian function fitted to the wake profile. **Characterization**: Performed simultaneously with the wake identification. **Automation**: Yes. **Flexibility**: Partial.
ATS	**Input data**: Radial velocity field, wind direction (optional), wind turbine locations. **Identification**: Threshold value from the intensity histogram. **Characterization**: Midpoints of the concentric arcs crossing the wake contour. **Automation**: Yes. **Flexibility**: Partial.

5 Proof of concept: Wake identification and characterization from the LES data

In this section, we demonstrate the performance of the ATS method in ~~the centerline detection~~application to the LES data and compare the result to the Gaussian method.

5.1 ~~LES wake detection~~

~~Unlike a 10-minute averaged LES wake, the instantaneous wake reveals more~~ An instantaneous LES wake reveals complex spatial features to be detected, although its intensity histogram remains rather smooth (Fig. 9b). The ATS method detects a continuous structure in the near wake and the beginning of the far wake, while the wake at $x/D > 10$ is represented as series of small disconnected structures (Fig. 12b-c). The ATS method does not capture the wake expansion, but only a trail of the low wind speed areas.

Since the ATS method extracts the outer contour of a shape, small holes inside the detected wake are automatically filled and do not affect the intersection-based centerline search (Fig. 13a). The current algorithm processes only the first continuous wake shape. Extending the centerline downstream requires a procedure to identify which of the small detected shapes actually belong to the far wake and the connection order. The former problem is more relevant for a lidar scan, which has less uniform background flow compared to the LES data.

Figure 13~~b compares the centerline and wake shape~~c compares the wake centerline and edges detected by the Gaussian and ATS methods. ~~Overall, the Gaussian method performs~~Both methods perform well in the range of ~~$2 < x/D < 10$. Additional errors may occur in the far wake~~$1 < x/D < 10$ and show good agreement on the same distance (Fig. 13c). Downstream $(x/D > 10)$, ~~where the wake~~the wake becomes weaker as it recovers to the free flow~~and~~. If the wake deficit function becomes too ~~weak~~flat to fit accurately~~.~~, the fitting result may place the wake center incorrectly or overestimate the standard deviation and, consequently, the wake width. The ATS method detects ~~a continuous structure in the near wake, while the far wake is represented as series of small disconnected structures (Fig. 13c)~~only disconnected structures in the far wake. Nevertheless, those structures primarily lie within the wake edges detected by the Gaussian method. The Gaussian centerline also passes through the centers of the ATS-detected structures. A good agreement between methods can be explained by the fact that the ATS method searches for regions of high intensity, i.e., low wind speed. At the same time, the Gaussian method approximates a wake center at the point of high wake deficit, which also corresponds to low wind speed.

~~Sample wake detection using idealized LES data. (a) Intensity histogram of an instantaneous flow field; (b) original data normalized to the range of 0, 1, (c) a thresholded image overlaid with the wake boundaries and centerline detected by the Gaussian method, and (d) color-coded wake shapes detected by the ATS method.~~

~~While the centerline extraction using image processing works well with the continuous shapes, correct identification of the downstream disconnected shapes as a part~~Overall, the Gaussian and ATS centerline search method show complimentary flaws. The Gaussian method may estimate the wake center correctly on a weak wake profile, but return a large standard deviation leading to an overestimation of the wake ~~requires further modification of the algorithm, that is not discussed in this study~~width.
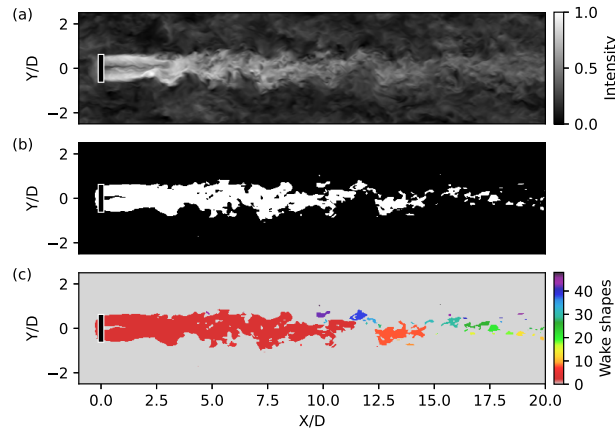
Figure 12. Wake and centerline identification for a sample instantaneous LES wake: (a) normalized flow field, same as Fig. 9b; (b) thresholded flow field; and (c) wake shapes color-coded to show connectivity.
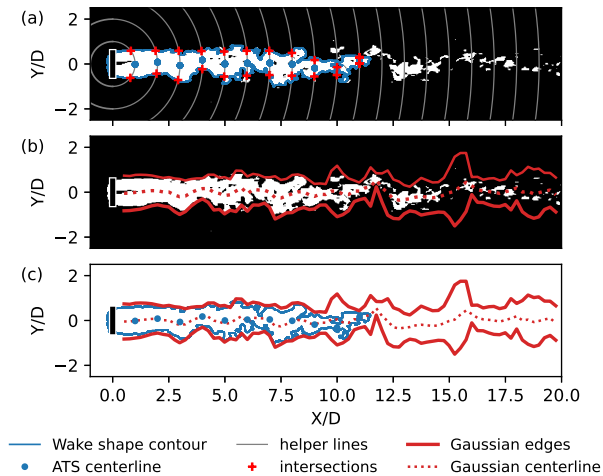

Figure 13. Sample wake identification and characterization using idealized LES data. (a) Thresholded data overlaid with the contour of the wake shape; (b) thresholded data overlaid with the wake boundaries and centerline detected by the Gaussian method; (c) ATS and Gaussian wake detection results, overlaid.

The Gaussian method does not always interpret strong wake meandering correctly and mistakes a wake turn for a wide wake. On the contrary, the ATS method is capable to discern a complex wake shape, but has problems with the centerline detection if the wake shape is too irregular due to wake merging or mixing with noise.

~~We have used the LES dataas a proof-of-concept to show the capability~~

28

6 Results

For the lidar data, we perform an extensive comparison to the manual wake identification and characterization and evaluate the accuracy of the ATS method. We further compare the performance of the ATS and Gaussian methods and discuss the application of the ATS method in the centerline detection. We show both ensemble statistics and demonstrate the methods performance on sample scans showing each of the most represented non-corrupted subsets: parallel, aligned wakes and bimodal.

6.1 Comparison of the ATS wake identification against the manual identification and deficit-based thresholding

We construct a confusion matrix to assess the performance of the methods for a single lidar scan. The 2×2 confusion matrix describes the comparison of the automatic thresholding methods (deficit-based or ATS, see Table 2) against the manual method and contains the following outcomes:

– True Positive (TP) – the point is detected as a wake point by both manual and automatic identification.

– True Negative (TN) – the point is detected as a free-flow point by both manual and automatic identification.

– False Positive (FP) – the point is detected as a wake point by the automatic method but is a free-flow point in the manual identification.

– False Negative (FN) – the point is detected as a free-flow point by the automatic method but is a wake point in the manual identification.

If the automatic identification is accurate with respect to the manual identification, TP and TN values tend to 100%, while FP and FN are close to zero.

The bimodal subset can be considered the most convenient for the manual threshold segmentation. It utilizes the strict criterion for the manual threshold that the wake shapes should not merge (Fig. 10d). In the example, the ATS method sets the threshold higher compared to the manual identification (Fig. 10e). Hence the far-wake area is slightly reduced. The deficit-based method (Fig. 10f) produces a similar result.

The aligned wakes subset utilizes the same manual threshold criteria for the wake splitting as the bimodal subset (Fig. 15), although the condition may be harder to fulfill. For some lidar scans, the far wake from the turbine AV10 and the near wake from AV7 cannot be separated, unless the threshold is increased so that the far wake is not identified (Fig. 15d). In this case, detecting a general shape of the wake takes the priority. The manual threshold is then more subjective than
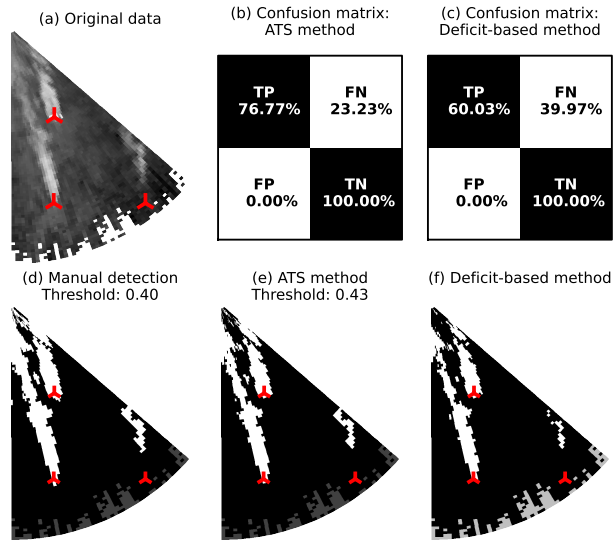
29

Figure 14. Scan #599 (bimodal subset), wake ~~detection~~identification. (a) The original data in the Cartesian coordinates; (b-c) confusion matrices for the ATS and deficit-based methods; (d) manual threshold selected in a way to separate the two wakes; and (e-f) thresholds estimated by the ATS and deficit-based methods.

that of the bimodal subset. The deficit-based method underestimates the threshold more significantly than in the bimodal case
590 and produces ~~a large~~ larger percentage of false ~~positive detections~~ positives than the ATS method (Fig. ~~14~~15f).

The parallel wakes subset is the most challenging, both for the manual ~~detection and~~ identification and the automatic methods (Fig. ~~15~~16). The wind direction in the subset is ~~close to~~ approaching 210°, ~~at which~~ where the crosswind effects start (Fig. 3) and noise appears at the border of a lidar scan. Unlike the corrupted scans with a high amount of non-physical wind speed values, the region ~~near~~ around the wind turbines AV7 and AV10 contains valid measurements and ~~allows to perform wake~~
595 ~~detection~~ still allows performing wake identification with relative success. However, the ~~detection~~ wake identification accuracy declines due to the border noise~~;~~, and only one wake can be extracted well enough to perform the analysis on the wake ~~direction~~ centerline and shape evolution. If the threshold is increased to distinguish wakes and noise, the wake from AV10 remains nearly undetected as can be seen from Fig. ~~15~~16d. The ATS method returns a lower threshold that improves distinguishing the shape of the AV10 wake but falsely detects noise ~~near~~ as a part of the AV7 wake (Fig. ~~15~~16e). The deficit-based method ~~significantly~~
600 ~~underestimates the threshold and generates too many false positives~~ estimates the threshold rather accurately, but may detect additional false positives near wind turbines (Fig. ~~15~~16f).

We ~~plot the thresholds predicted by the wake deficit and ATS methods against the manual segmentation~~ summarize the comparison of true negative and true positive detections in the box plots (Fig. 16)~~. The deficit-based threshold is primarily used to detect wakes from LES or PIV data (España et al., 2011). The lidar data has less uniform free flow and lower resolution. This~~
605 ~~results in a relatively poor correlation with the manual segmentation – the deficit-based threshold is always underestimated. Therefore, more points, including noise points, might be falsely detected as wake points.~~
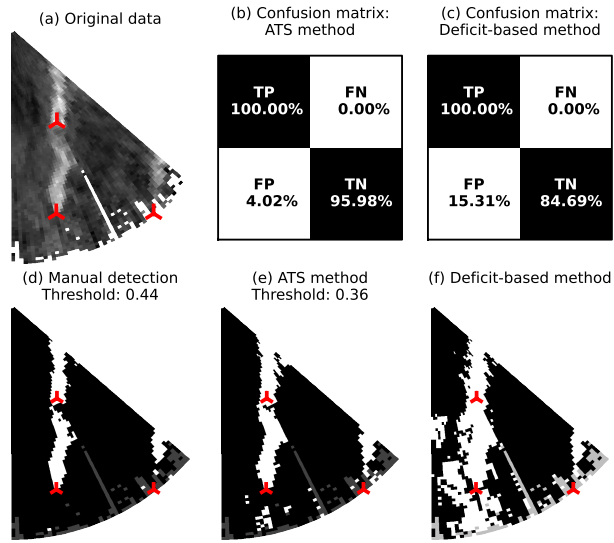
30

Figure 15. Scan #221 (aligned wakes subset), wake ~~detection~~identification. (a) The original data in the Cartesian coordinates; (b-c) confusion matrices for the ATS and deficit-based methods; (d) manual threshold selected in a way to separate the two wakes~~as much as possible~~; and (e-f) thresholds estimated by the ATS and deficit-based methods.
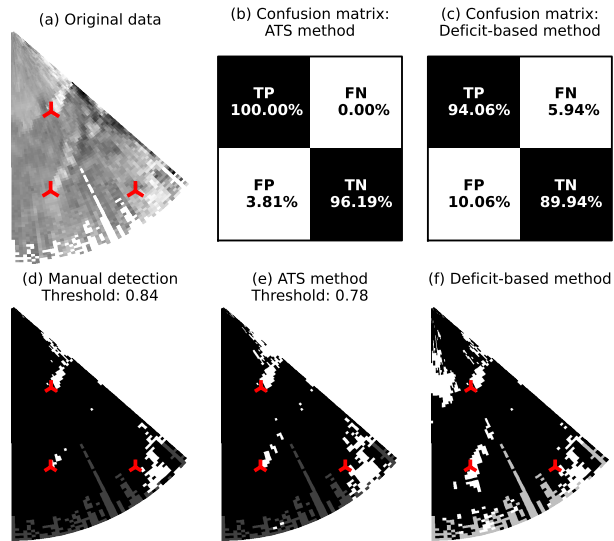

Figure 16. Scan #60 (parallel wakes subset), wake ~~detection~~identification. (a) The original data in the Cartesian coordinates; (b-c) confusion matrices for the ATS and deficit-based methods; (d) manual threshold selected in a way to reduce noise but keep a general shape of the wakes; and (e-f) thresholds estimated by the ATS and deficit-based methods.
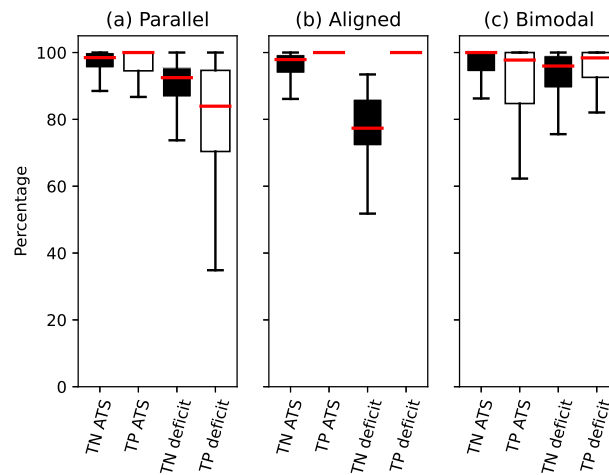
Figure 17. Ensemble statistics of true negative and true positive detections within the subsets.

17) for the different subsets.

~~The~~ Due to the amount of noise, the parallel wakes subset is challenging for both methods. Nevertheless, the ATS method approaches manual identification rather effectively, while the deficit-based ~~thresholds form two clusters in the threshold plot~~ method leaves a decent amount of noise which may alter the identified wake shape (Fig. 16f).

Both methods score nearly 100% for the true positive detections in the aligned subset (Fig. ~~16a~~17b). The ~~parallel and aligned wake subsets share similar behavior and return a threshold significantly lower than manual-detected threshold. In the bimodal case, the deficit-based threshold shows better agreement with the manual-detected threshold but not as good as the ATS-based threshold(Fig. 16b). Overall, the deficit-based method consistently underestimates the~~ result is caused by the criterion for the manual threshold: separate two different wakes. The criterion is too strict for both automatic methods to achieve, therefore, they always underestimate the threshold~~, implying that the 5% criteria should be changed to improve the detection result. The ATS method performs on par with the manual detection. The strongest discrepancy between the manual and ATS methods can be seen for the aligned wakes subset, in which the outliers might be partially caused by the ambiguity of~~ . Still, the ATS method gets closer to the manual threshold, which is reflected in lower variation of true negative detections compared to the ~~manual detection criteria~~ deficit-based threshold.

The deficit-based and ATS wake identifications behave rather similar for the bimodal subset (Fig. 17c) with respect to the manual wake identification. The variations in the bimodal subset are primarily caused by the wakes forming in lidar near range, which is scanned at higher resolution than the rest of a scan. I.e., any small threshold change affects more points at the wake edges than it would for the parallel or aligned subsets and results in stronger fluctuations in TP-FN values.

To reduce the influence of ambiguity of the manual detection, we construct a confusion matrix for each subset of 25 consecutive lidar scans instead of single scans. The corrupted scans are excluded from the comparison, since high noise prevented

Table 3. Comparison of the thresholding methods' performance against the manual wake identification

Data type	Subset	Scans	Manual-deficit, %				Manual-ATS, %			
			TP	FN	FP	TN	TP	FN	FP	TN
Parallel wakes	3	51−75	55	45	5	95	80	20	2	98
	4	76−100	69	31	4	96	97	3	4	96
	5	101−125	76	24	9	91	91	9	4	96
	6	126−150	85	15	9	91	95	5	4	96
	7	151−175	96	4	23	77	98	2	3	97
	11	251−275	95	5	22	78	99	1	4	96
	12	276−300	71	29	7	93	93	7	2	98
	16	376−400	80	20	6	94	96	4	3	97
Transitional	17	401−425	93	7	19	81	87	13	0	100
Aligned wakes	8	176−200	99	1	28	72	98	2	1	99
	9	201−225	100	0	13	87	100	0	10	90
	10	226−250	100	0	23	77	98	2	3	97
Bimodal	17	426−450	88	12	2	98	82	18	0	100
	18	451−475	83	17	1	99	89	11	0	100
	19	476−500	97	3	5	95	96	4	4	96
	20	501−525	97	3	7	93	85	15	2	98
	21	526−550	99	1	15	85	90	10	5	95
	22	551−575	100	0	20	80	90	10	8	92
	23	576−600	85	15	2	98	94	6	4	96

the manual detection for most of the scans. Table ~~2~~ 3 summarizes the detection outcomes for each subset. The ATS and deficit-based method ~~often underestimates the threshold, therefore the share of true positive detections is nearly always 100%~~ perform comparably in terms of true positives in the aligned and bimodal subsets. However, the amount of ~~true negatives~~ false positives for the deficit-based method indicates a high probability of identifying noise as a wake. Additionally, the percentage of ~~true negative detections~~ false positives strongly fluctuates within the same type of the subset making the fixed threshold method unreliable.

While the amount of true positives for the ATS method may drop to 80% for a complex subset, the amount of true negatives consistently stays near 95% – the background flow is mostly detected correctly regardless of the subset type, which is ~~a significant~~ an improvement compared to the deficit-based method. Compared to the manual detection, the ATS method does not always separate wake and noise correctly, particularly for the parallel wakes subset (Fig. ~~15~~16) and thus requires additional

filtering. For the aligned and bimodal subsets, the ATS method is capable to detect the general wake shape rather similar to the manual detection.

It should be noted that the deficit-based wake identification requires a free-flow wind speed to define the threshold and an additional preprocessing of a lidar scan – a correction based on the wind direction or a more complex lidar retrieval method. The ATS method runs solely on the lidar data and does not require information besides what is already contained in a lidar scan.

6.2   ~~Centerline detection~~Comparison of the wake characterization using Gaussian and ATS methods

We perform ~~centerline detection using~~ the wake characterization by searching for the wake centerline from the thresholded image produced with the ATS method as described in Sect. 4.2 ~~and~~ or by applying the Gaussian method as described in Sect. 4.3. ~~Both methods are compared~~ First, we provide a comparison of selected scans against the manual wake ~~detection~~ characterization from the lidar scan image as described in Sect. 4.5. ~~We compare the found centerlines~~ The found centerlines are compared by fitting the regression lines to the relative coordinates, so that each local coordinate system is centered at a selected wind turbine.

The parallel wakes subset (Fig. ~~17~~18) contains a short but ~~contrast~~ pronounced wake from the wind turbine AV7 and a ~~longer~~ long weaker wake from the wind turbine AV10. ~~Due to the fact that~~ Since the AV10 wake is frequently detected as series of small disconnected structures, the current ATS method detects the centerline only ~~in~~ for the first continuous shape, which rarely extends beyond the near-wake region. The manual and Gaussian ~~detection~~ wake characterization can be carried further into the far-wake region, but become rather uncertain as the far wake recovers to the free flow or mixes with the border noise. Considering the problems that the border noise poses for the wake identification in less clean scans (Fig. 16), the characterization outcome can be improved by excluding the near-border sector of $1-2°$ width from the identification process.

The aligned wakes subset (Fig. ~~18) possesses~~ 19) shows a distinctive feature: the wakes are aligned along the line connecting two wind turbines resulting into the merge of the AV10 far wake and the AV7 near wake. Additionally, the connecting line is parallel to the Y-axis in ~~the Cartesian coordinates(Fig. 2)~~Cartesian coordinates, so the centerline tends to $X = $ const when the wakes are perfectly aligned. Hence, the coefficient of determination R^2 either approaches zero or becomes negative and does not indicate the quality of the regression fit.

The bimodal subset (Fig. ~~19~~20) has the longest wakes in the data set. The wake ~~detection~~ identification in the far wake (i.e. lidar near range) is hindered by wake merging and the narrowness of the scanned area. For example, the ATS method may underestimate the threshold and detect merging wakes as a single shape. The ATS-based threshold can be adjusted to guarantee the wake splitting. The adjustment is performed automatically by increasing the threshold with an increment of 0.05 until the stopping ~~criteria~~ criterion – the wind turbines belong (or are located near) to different wake shapes – is reached.

The merging wakes also affect the accuracy of the Gaussian method, ~~in turn,~~ as it may detect a wake center incorrectly because of high wake deficit in the neighboring wake. The ~~detection~~ characterization inaccuracy in the lidar near range is compensated by higher overall number of data points available for fitting, compared to the other subsets.
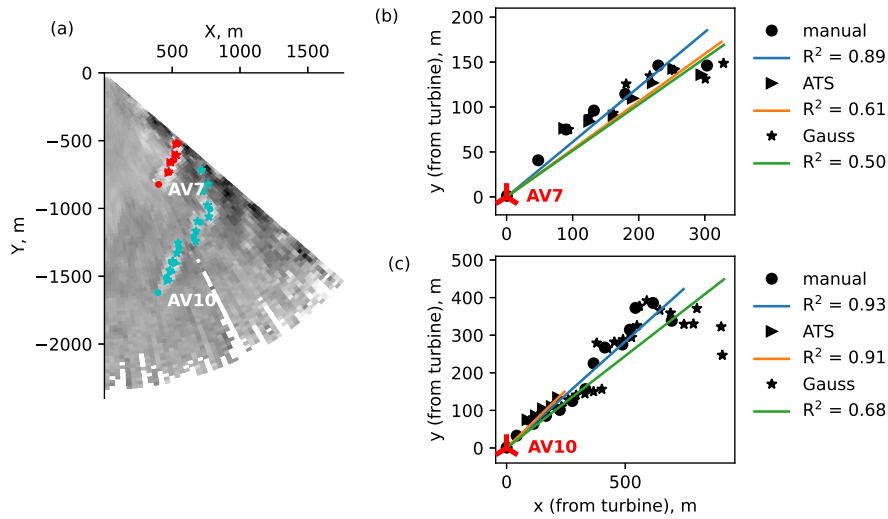
Figure 18. Scan #59 (parallel wakes subset). (a) An overview of the detected centerlines and regression fits for (b) AV7 and (c) AV10.
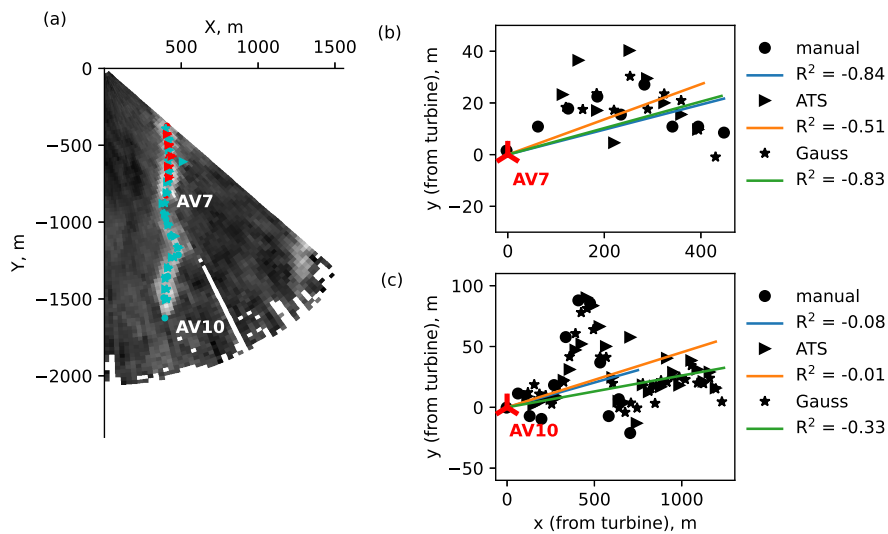

Figure 19. Scan #221 (aligned wakes subset). (a) An overview of the detected centerlines and regression fits for (b) AV7 and (c) AV10.

670 ~~Both methods perform best for the long wakes in a lidar scan with low noise and show a good agreement on the detected centerlines. When the far-wake region cannot be detected properly, the methods still agree in the near wake. For noisy subsets, such as parallel wakes, the performance of all methods strongly relies on the data quality. The longer the near wake can be detected, the higher is the accuracy of the centerline detection. The ATS method requires additional algorithm to identify downstream disconnected structures as a part of the wake.~~
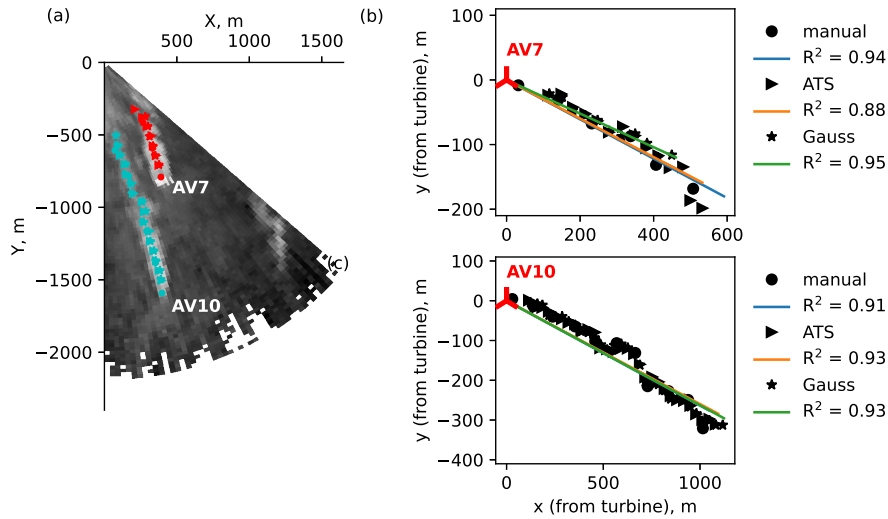
Figure 20. Scan #599 (bimodal subset). (a) An overview of the detected centerlines and regression fits for (b) AV7 and (c) AV10.
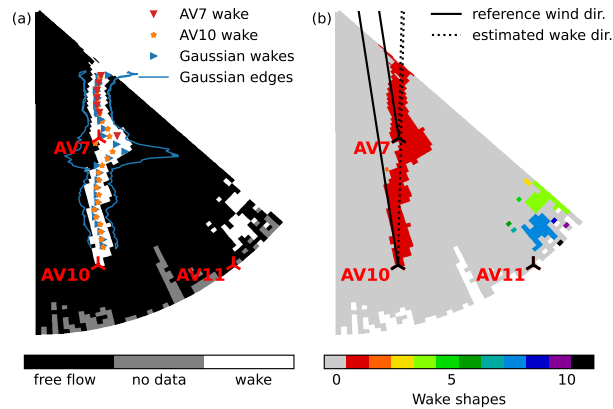

Figure 21. Scan #222 (aligned wakes subset) sample wake ~~detection~~ identification and characterization showing (a) comparison of the ATS and Gaussian methods, (b) ~~shapes detected~~ wakes identified by the ATS method after the threshold is applied, and wind and wake direction.

6.3 ~~Comparison of the Gaussian and ATS methods~~

675

~~Figure 20~~ Figure 21 shows an example of wake ~~detection~~ identification performed on a lidar scan from the aligned wakes subset. The subset is characterized by the wake merging near AV7. The formed structure proves to be challenging for a Gaussian method, as the centerline point and far-wake width for AV10 are estimated incorrectly.

The ATS method detects wakes as a single shape. Unlike the bimodal subset, the merging wakes in the aligned wake subset

680 do not necessarily worsen the performance of the centerline detection method. The centerline is first detected for the AV10

36

Table 4. Rules for scoring Gaussian and ATS centerline search methods performance.

Score	Gaussian method	ATS centerline search
0	The method failed to find the wake at all or less than 10% of the visible wake was identified.	
0.5	The centerline loosely matches the wake centerline, but the wake width is overestimated or undefined.	The wake shape is readable from the thresholded image, but the centerline is incomplete or erroneous.
1	The method had correctly identified at least 75% of the visible wake and its centerline.	

wake, from which the wake direction can be estimated. Since the wakes are merged, the centerline detection for AV10 continues in the AV7 wake. The centerline search for AV7 starts at the corresponding turbine location and is performed in the direction of the AV10 wake, thus excluding the merge region from the search. Thus the centerline of the AV7 wake gets detected twice if no stopping ~~criteria~~ criterion (e.g., the AV10 centerline passes AV7 location) is activated. Both detected centerlines agree in the AV7 wake region and follow the Gaussian centerline rather well. Near-border wake centers of the AV7 wake deviate from the presumed centerline because border noise is erroneously attributed as a part of the wake. ~~Considering the problems the border noise may pose for the wake detection in less clean scans~~

When it comes to the comparison of wake characterization over the whole data set, the effect of weak wakes or merging on the Gaussian method performance complicates a direct comparison. Due to the errors, the Gaussian centerline cannot be taken as a 'true' value and requires verification on its own.

Instead, we perform a visual comparison of the Gaussian and ATS centerline search methods to score their success rate. The performance of both methods rather differs along the wake, therefore we evaluate the detection result on two segments: $l \leq 4D$ and $l > 4D$ from the wind turbine. The $l \leq 4D$ segment usually covers the most well-resolved part of the wake in non-corrupted scans, we attribute it as the near wake. The rest of the wake would be then referred as the far wake and characterized by lower wake deficit. Next, we score the success rate based on whether the method was able to identify both wake shape and centerline, failed on one of the tasks, or did not distinguish the wake at all (Table 4).

As mentioned for the LES wake identification and characterization (Sect. 5), the ATS and Gaussian methods are prone to errors in different aspects. A partial success for the Gaussian method would usually mean a centerline estimated with a large standard deviation, while a partial success for the ATS method would be the detection of the wake shape, but not the full centerline.
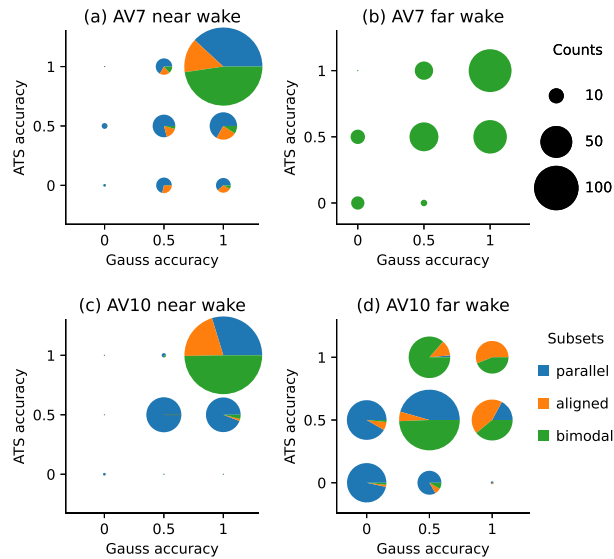
Figure 22. Overview of the Gaussian and ATS method performance on the wake detection and characterization.

A summary for the data set excluding corrupted scans is presented in Fig. 22 by showing the counts for each outcome and their distribution between the subsets.

The near wakes are well resolved and show a high number of outcomes where both methods succeed. The partial detections are spread differently. The non-perfect outcomes for the AV7 near wake are spread rather equally (Fig. 22a). The increased error rate of the ATS method in the AV7 near wake is caused either by strong border noise (parallel subset) or strong upstream wake influence (aligned subset) – both distort the detected wake shape.

Due to the studied wind directions, the AV10 near wake is not subjected to the upstream turbine influence. The wake is very clear and poses problems mainly for the ATS method in the parallel subset, when it cannot be identified as a continuous shape. Hence, the ATS method under-performs and stops at the wake identification, while the Gaussian method can succeed in both aspects (Fig. ~~15)~~22c).

The comparison of AV7 far wake accuracy (Fig. 22b) is relevant only for the bimodal subset, where the corresponding wake reaches the required length. Detection outcomes for the AV7 far wake follow a pattern that resembles the other cases: very low counts of partial or full success when one of the methods fails, higher counts for partial and full success of both methods.

The exception from this pattern is the AV10 far wake (Fig. 22d). Both methods achieve partial success most often. The decreased success rate is primarily caused by the wake merging in bimodal and aligned subsets. When it comes to the parallel wake subset, both methods are likely to fail. The weak AV10 far wake limits efficiency of both methods: the threshold is not enough to separate the wake from the free flow and the fitting cannot be carried on to the nearly flat wake deficit function.
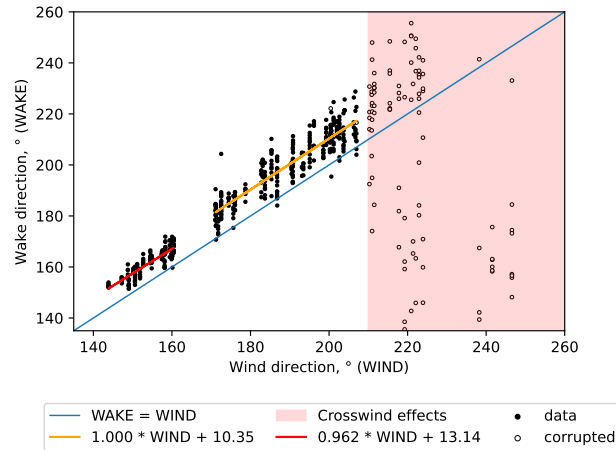
Figure 23. Comparison ~~of the~~ between reference wind direction (WIND) and estimated wake direction (WAKE).

The low count of (0, ~~excluding the near-border sector of~~ 1 ~~— 2 width from the detection should improve the outcome~~) pairs throughout the comparison indicates that none of the methods outperforms another in any part of the wake. If one method fails, the other usually fails too or achieves only a partial success.

6.3 Wind and wake direction

The regression line fitted to the ATS-detected centerline also indicates the wake direction. A strong mismatch between reference wind direction and wake direction can be seen for most lidar scans from the data set (Fig. ~~20~~21b).

Comparing the directions for the whole data set, we observe a clear trend for the wake direction deviating clockwise from the reference wind direction until the crosswind effects start at 210° (Fig. ~~21). The trend continues for the reference wind direction above 210 for the corrupted lidar scans, where wake detection was still possible despite the erroneous data.~~ 23).

The valid points for the reference wind directions less than 210° group into two distinct clusters (Fig. ~~21~~23). The leftmost cluster corresponds to the bimodal subset and lies within the range of wind directions of 140−170°. Another cluster contains the results for the aligned, transitional, and parallel wakes subsets and covers the range of wind directions of 170−210°. Fitting a linear regression to each group returns a similar slope but a different intercept value. Although the fitted line slope is not equal to one, the regression fit on the selected range shows a nearly constant offset between wind and wake direction with the bimodal subset having noticeably lower difference, than other subsets.

The vertical veer and clockwise rotation of the wake in the Northern hemisphere due to the Coriolis force are known effects causing wake rotation and were confirmed by ~~in situ~~ observations and LES studies of ~~the~~ wind farms (Magnusson and Smedman, 1994; Abkar and Porté-Agel, 2016; van der Laan and Sørensen, 2017). The wind turbine AV7, closest to the lidar, is scanned nearly at the hub height, while the farther wind turbines, AV10 and AV11, are scanned near the top-tip height (Fig. 1). Due to the elevation and vertical veer, the wind and wake direction discrepancy is the strongest for AV10 and AV11.
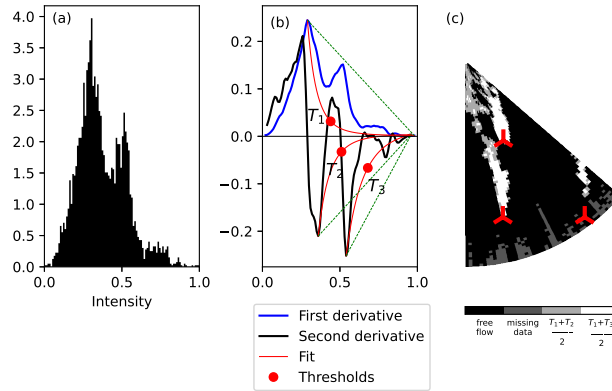
Figure 24. Scan #553 (bimodal subset). (a) Intensity histogram of the normalized data, (b) the ATS method search for the thresholds, (c) thresholded image.

Nevertheless, we also observe a deflection for the near wake of AV7, although the noticeable effects of the Coriolis force are usually recorded for the downwind distance of $6D$ or higher. The additional discrepancy can be explained by the yaw mis-alignment (Bromm et al., 2018), reference measurements uncertainty (Gaumond et al., 2014), and the lidar installation's imperfection. The ~~discrepancy~~ wake direction variation for the bimodal subset ~~could be~~ (reference wind direction $140-160°$) was possibly reduced because of the longer wakes and, consequently, more precise ~~regression fit~~estimation of the wake direction. We do not have additional data to distinguish these factors and leave it for a future study.

The outliers showing strong differences between wind and wake direction highlight the lidar scans where the wake ~~detection~~ identification and characterization was hindered by noise or strong irregularity of the wake~~shape~~. The wind-wake direction plot can be used for diagnostic purposes to select the lidar scans that require additional processing prior to ~~wake detection~~the wake identification.

6.4 ~~Near and far wake separation with a threshold~~Wake identification in the bimodal subset using the ATS method

~~Bimodal subsets~~ Bimodal subsets often have a distinctive double peak in the intensity histogram ~~, which results into two local minimums in the second derivative graph~~(Fig. 24a). The highest histogram peak corresponds to the free flow. The second peak forms due to a long far wake from AV10 and subsequent merging of the two wakes.

The double peak from the histogram translates into two local minimums in the second derivative graph (Fig. 24b). The occasions of two local maximums in the first derivative were rarer in the regarded data set. Applying the ATS method to both second derivative minimums provides a unique opportunity to estimate two thresholds T_2 and T_3 in addition to the threshold T_1 from the first derivative. The final threshold values either separate the full wake from the free flow ($(T_1 + T_2)/2$) or extract only the most intense part of the wake ($(T_1 + T_3)/2$) (Fig. 24c). The splitting point falls approximately at the downstream distance of $4-5D$, marking a transition from the near to far wake.

We ran the ATS method without subset-specific parameters meaning that it always estimated only one threshold for the wake identification. During the threshold estimation (Sect. 4.1), the current algorithm selects the global maximum or minimum of
760 the first and second derivatives, respectively. The free-flow histogram peak usually results in the global maximum of the first derivative in our data set and does not affect the performance of the ATS method. However, the local minimum values of the second derivative appear to be more sensitive to the intensity distribution. Relying on the global minimum may lead to selecting a stricter threshold T_3 (Fig.24b). A strict threshold does not detect most of the far wake, as shown in Fig.24c.

A less strict threshold T_2 could be chosen based on the proximity to T_1 as a control value. However, it would require an
765 automatic check whether another local minimum can produce a valid threshold. The implementation posed a challenge, if the current algorithm ran without subset-specific parameters, and produced erroneous threshold estimation for other scans. We refrained from using more complex approach in the bimodal subset for now. The current ATS method, therefore, overestimated the threshold and did not identify the full wake in about 8% of the bimodal cases.

7 Conclusions

770 We ~~proposed an automatic thresholding method for the wake detection based on the image processing method for the whitecaps detection on the ocean surface. We also described an automatic method to detect the wake centerline from an irregular wake shape. The results showed that image processing techniques were also a viable solution for wake detection and did not strongly depend on the supplementary measurements , such as reference~~ developed a set of methods to analyze lidar scans for wake identification and characterization. During the study, we focused on the procedures that would automatically process
775 a large data set and primarily rely on the information contained in the lidar data or site characteristics such as lidar and wind turbine positions. To structure the analysis of the results, we split our data set into several subsets grouping the scans with similar characteristics. While the classification could be performed based on the wind direction or visual inspection, we introduced entropy as criterion to reflect the flow characteristics. When calculated in the azimuthal or radial direction, Shannon entropy is sensitive to the disturbances caused by wakes and allows scan classification if the wind direction is unknown. The
780 entropy values also highlighted the lidar scans that were unsuitable for the analysis due to the high amount of non-physical measurements caused by the crosswind effects. The classification by entropy criteria introduced in the study was not yet used to apply scan-specific corrections during the thresholding.

An existing automatic thresholding method, the deficit-based method as referred in the study, thresholds the wind speed data at 95% of the free-flow wind speed and ~~direction. The preprocessing tools developed alongside the wake detection method~~
785 ~~helped to recognize the lidar scans that are not suitable for the analysis. The same tools allowed to group the valid scans into subsets~~ was initially suggested for more regular wind tunnel wakes. The reliance on the actual wind speed hinders the deficit-based method performance on the lidar data – a retrieval procedure should be applied to the measured radial velocity to reconstruct the wind field. Additionally, the fixed ratio of 95% does not regard the quality of a lidar scan. To overcome these disadvantages, we proposed an automatic thresholding method for wake identification, the ATS method, based on the
790 ~~expected features. Future plans include testing the preprocessing tools on a larger data set to completely remove dependency~~

~~on the supplementary dataand visual analysis for the filtering and classification~~method for whitecaps detection on the ocean surface. The method did not require the knowledge of the actual wind speed and could be applied to the radial velocity data. The preparatory step applied normalization through scaling data to the range of $[0,1]$, thus requiring the removal of outliers during the lidar scan preprocessing.

795 The comparison to the manual thresholding showed that the ATS method generally ~~agreed well~~ performed better than the deficit-based method and on the par with the manual ~~threshold selection. We also compared the ATS method against~~ wake identification, which opened a possibility to use it when manual thresholding is infeasible.

We also described an automatic method for the wake centerline search from the thresholded data. The centerline search could run without wind direction provided by making a rough approximation of the wake direction. However, the current 800 algorithm processes only the first continuous shape limiting the application to the wind fields with little noise obstructing the wake identification.

We compared the centerline found from the thresholded data to the Gaussian fit method. Although the Gaussian method ~~performed~~ performance on the lidar scans ~~was~~ not as good as on the LES data, the ~~detections~~ wake characterization in the near-wake region showed ~~a good~~ an agreement between the methods with ~~the~~ respect to the manual centerline detection. At the 805 same time, the accuracy of both Gaussian and ~~ATS~~ ATS-based methods decreased in the far-wake region, especially for noisy data or in the case of wake-wake interaction. In the latter case, the ATS method often ~~detected~~ identified two wakes as a single shape~~. To perform a centerline detection, we adjusted a threshold to split the wakes. The separation of wake and false positives remained an open problem and left room for improving the ATS method in the~~, affecting the centerline search algorithm. The algorithm performs better when the wake directly hits the downstream wind turbine – the merged wakes can be considered as 810 one wake and have a common centerline. When the wakes are forming side by side and get close to each other, the threshold may need additional adjustment until the identified wake shape is split.

The results showed that automatic thresholding from the intensity histogram was viable for the wake identification not only for the LES but also lidar data. We see a potential to improve the wake characterization algorithm to detect the centerline of the whole wake and plan to present it in future studies.

815 *Code and data availability.* The Python code for wake identification using ATS method, centerline detection and a sample lidar data set are available upon request.

Video supplement. The video https://doi.org/10.5446/54055 demonstrates wake identification results for all lidar scans in the data set. No post-processing is performed after running the ATS algorithm.
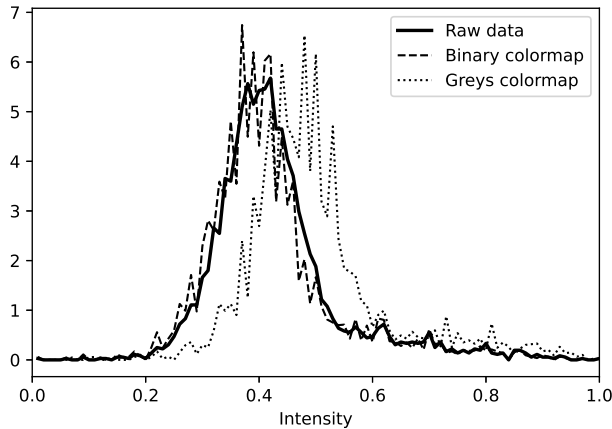
Figure A1. Comparison of the intensity distribution in the original (raw) data and image plotted using Python Matplotlib with different grayscale colormaps.

Appendix A: Image data processing

820 An image has several properties which may affect the algorithm performance compared to the use of the raw wind speed data:

1. Image resolution in dots-per-inch (dpi): the resolution of 72 dpi transforms an original data point into an image pixel as 1-to-1 approximately. Higher resolution increases the number of pixels per data point. Lower resolution merges several data points into one pixel.

2. Colormap: the ATS method relies on the image grayscale intensity as an input. A non-grayscale image can be desaturated,
825 but the colormap of the original image then should be sequential rather than perceptually uniform or diverging. For the latter, the conversion to the grayscale gradually reduces the contrast between high and low values making the ~~detection~~ wake identification impossible. Additionally, several grayscale colormaps exist. Depending on the colormap, the ~~image intensity histogram~~ intensity histogram of an image may shift to the left or right compared to the raw data. We observed this effect when the 'Greys' colormap of the Python Matplotlib library was used. This colormap emphasizes light tones;
830 as a result, the intensity histogram peak slightly shifts to the right, although the general shape of the peak is preserved (Fig. ~~23~~A1). The colormaps 'binary' or 'gray' from the same library return the result that follows the original data.

3. ~~The image~~ Image intensity: as processed by Python, the values are rounded up to second digits and some are assigned to different bins compared to the original data. The histogram and CDF have stronger oscillations than the raw data (Fig. ~~23~~A1) and require smoothing before the ~~ATS method can be applied~~application of the ATS method.

835 Running an automated threshold detection on the image raises another question: how much does the image resolution affect the ~~detection~~ identification accuracy compared to the raw data. We apply the ATS algorithm to raw and image data under different resolutions: 72, 150, and 300 dpi. We observe little influence from the image resolution, except for few LES cases,
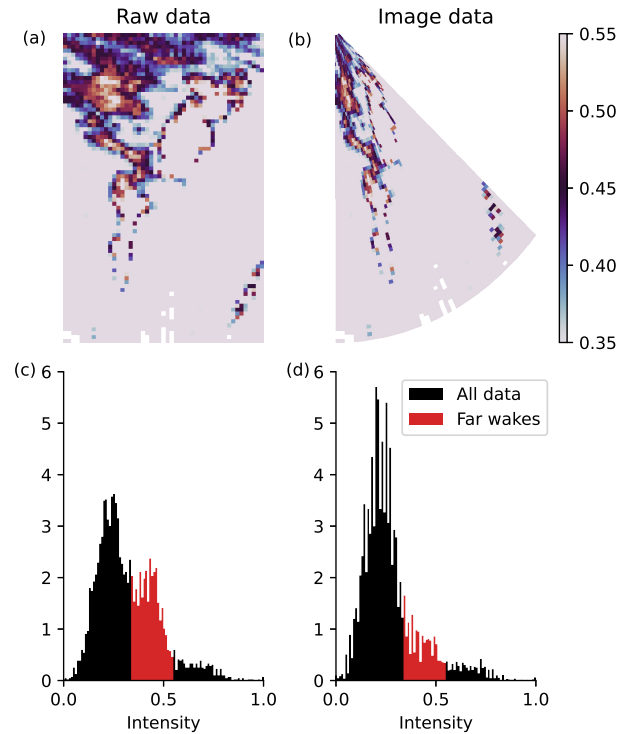
43

Figure A2. (a-b) Normalized wind speed data with far wakes highlighted and (c-d) corresponding grayscale intensity histograms of the lidar scan #551.

where the low resolution of 72 dpi affected the threshold detection. In those cases, the detected threshold is lower than in fine resolution cases, and, therefore, a larger shape is identified as a wake. The image resolution of 150 dpi and above agrees well

840   with the wake ~~detection~~ identification from the raw data. The general shape of an image intensity histogram does not depend on the image resolution. The image resolution of 150 dpi or higher is recommended for use, although 72 dpi also produces good detection results.

In the case of lidar measurements, the ~~detection~~ wake identification from the image data can be performed in two ways: by plotting the original data either in polar or Cartesian coordinates. The ~~detection~~ wake identification from the polar coordinates

845   image does not bear a ~~significant~~ notable difference from the raw data~~detection. After the conversion to~~, apart from the aforementioned specifics of the image resolution and intensity. However, if the lidar data are plotted in the Cartesian coordinates as a scanned sector, the lidar close and far range get distorted, affecting the percentage of the area covered by the wakes and, consequently, the histogram shape.

The effect is most pronounced when the wind blows towards the lidar. As described in the subsets overview in Sect. **??**, this

850   wind direction and wake behavior result in the bimodal intensity histogram. The leftmost, high peak, contains points from the free flow, while the second, low, peak accumulates points from the far wake. The second peak gets smoothed when the input

data ~~is~~ are changed from the normalized wind speed to the grayscale image plotted in Cartesian coordinates. As can be seen from the comparison (Fig. ~~24~~A2), the lower peak corresponds to the data in the lidar's close range. After the conversion to the Cartesian coordinates, the close range area shrinks significantly, while the free-flow area on the far lidar range enlarges. The transition between coordinate systems changes the balance between wake and free-flow pixels and virtually increases the share of the latter.

~~(a-b) Normalized wind speed data with far wakes highlighted and (c-d) corresponding grayscale intensity histograms of the lidar scan #551.~~

Author contributions. MK adapted the image processing algorithm developed by MBP to the wake identification, expanded the algorithm with the centerline characterization code and performed analysis of the wake identification and characterization. MBP provided further guidance on the image processing techniques. JR provided information on the lidar setup and explanation on the discrepancies between reference and lidar data. FGN consulted on the method practical application. All authors had contributed to the proofreading and correcting the article draft.

Competing interests. The authors declare that they have no conflict of interest.

References

Abkar, M. and Porté-Agel, F.: Influence of the Coriolis force on the structure and evolution of wind turbine wakes, Phys. Rev. Fluids, 1, 1–14, https://doi.org/10.1103/physrevfluids.1.063701, 2016.

Ahsbahs, T., Nygaard, N. G., Newcombe, A., and Badger, M.: Wind Farm Wakes from SAR and Doppler Radar, Remote Sens., 12, 462, https://doi.org/10.3390/rs12030462, 2020.

Ainslie, J.: Calculating the flowfield in the wake of wind turbines, J. Wind Eng. Ind. Aerodyn., 27, 213–224, https://doi.org/10.1016/0167-6105(88)90037-2, 1988.

Aitken, M. L., Banta, R. M., Pichugina, Y. L., and Lundquist, J. K.: Quantifying Wind Turbine Wake Characteristics from Scanning Remote Sensor Data, J. Atmos. Ocean. Technol., 31, 765–787, https://doi.org/10.1175/JTECH-D-13-00104.1, 2014.

Bakhoday-Paskyabi, M., Reuder, J., and Flügge, M.: Automated measurements of whitecaps on the ocean surface from a buoy-mounted camera, Methods Oceanogr., 17, 14–31, https://doi.org/10.1016/j.mio.2016.05.002, 2016.

Bastine, D., Witha, B., Wächter, M., and Peinke, J.: Towards a Simplified DynamicWake Model Using POD Analysis, Energies, 8, 895–920, https://doi.org/10.3390/en8020895, 2015.

Beck, H. and Kühn, M.: Reconstruction of three-dimensional dynamic wind-turbine wake wind fields with volumetric long-range wind doppler LiDAR measurements, Remote Sens., 11, https://doi.org/10.3390/rs11222665, 2019.

Bromm, M., Rott, A., Beck, H., Vollmer, L., Steinfeld, G., and Kühn, M.: Field investigation on the influence of yaw misalignment on the propagation of wind turbine wakes, Wind Energy, 21, 1011–1028, https://doi.org/10.1002/we.2210, 2018.

Chamorro, L. P. and Porté-Agel, F.: Effects of Thermal Stability and Incoming Boundary-Layer Flow Characteristics on Wind-Turbine Wakes: A Wind-Tunnel Study, Boundary-Layer Meteorol., 136, 515–533, https://doi.org/10.1007/s10546-010-9512-1, 2010.

Doubrawa, P., Quon, E. W., Martinez-Tossas, L. A., Shaler, K., Debnath, M., Hamilton, N., Herges, T. G., Maniaci, D., Kelley, C. L., Hsieh, A. S., Blaylock, M. L., Laan, P., Andersen, S. J., Krueger, S., Cathelain, M., Schlez, W., Jonkman, J., Branlard, E., Steinfeld, G., Schmidt, S., Blondel, F., Lukassen, L. J., and Moriarty, P.: Multimodel validation of single wakes in neutral and stratified atmospheric conditions, Wind Energy, p. we.2543, https://doi.org/10.1002/we.2543, 2020.

España, G., Aubrun, S., Loyer, S., and Devinant, P.: Spatial study of the wake meandering using modelled wind turbines in a wind tunnel, Wind Energy, 14, 923–937, https://doi.org/10.1002/we.515, 2011.

Fleming, P. A., Gebraad, P. M., Lee, S., van Wingerden, J. W., Johnson, K., Churchfield, M., Michalakes, J., Spalart, P., and Moriarty, P.: Evaluating techniques for redirecting turbine wakes using SOWFA, Renew. Energy, 70, 211–218, https://doi.org/10.1016/J.RENENE.2014.02.015, 2014.

Foti, D., Yang, X., Guala, M., and Sotiropoulos, F.: Wake meandering statistics of a model wind turbine: Insights gained by large eddy simulations, Phys. Rev. Fluids, 1, 044 407, https://doi.org/10.1103/physrevfluids.1.044407, 2016.

Gaumond, M., Réthoré, P.-E. E., Ott, S., Peña, A., Bechmann, A., and Hansen, K. S.: Evaluation of the wind direction uncertainty and its impact on wake modeling at the Horns Rev offshore wind farm, Wind Energy, 17, 1169–1178, https://doi.org/10.1002/we.1625, 2014.

Herges, T. G., Maniaci, D. C., Naughton, B. T., Mikkelsen, T., and Sjöholm, M.: High resolution wind turbine wake measurements with a scanning lidar, in: J. Phys. Conf. Ser., vol. 854, p. 012021, IOP Publishing, https://doi.org/10.1088/1742-6596/854/1/012021, 2017.

Howard, K. B., Singh, A., Sotiropoulos, F., and Guala, M.: On the statistics of wind turbine wake meandering: An experimental investigation, Phys. Fluids, 27, 075 103, https://doi.org/10.1063/1.4923334, 2015.

Krishnamurthy, R., Reuder, J., Svardal, B., Fernando, H. J., and Jakobsen, J. B.: Offshore Wind Turbine Wake characteristics using Scanning Doppler Lidar, Energy Procedia, 137, 428–442, https://doi.org/10.1016/j.egypro.2017.10.367, 2017.

Larsen, G. C., Aagaard Madsen, H., and Bingoel, F.: Dynamic wake meandering modeling, 2007.

910   Larsen, G. C., Madsen, H. A., Thomsen, K., and Larsen, T. J.: Wake meandering: a pragmatic approach, Wind Energy, 11, 377–395, https://doi.org/10.1002/we.267, 2008.

Lee, S., Churchfield, M., Moriarty, P., Jonkman, J., and Michalakes, J.: Atmospheric and Wake Turbulence Impacts on Wind Turbine Fatigue Loadings, in: 50th AIAA Aerosp. Sci. Meet. Incl. New Horizons Forum Aerosp. Expo., American Institute of Aeronautics and Astronautics, Reston, Virigina, https://doi.org/10.2514/6.2012-540, 2012.

915   Long, D. and Singh, V. P.: An entropy-based multispectral image classification algorithm, IEEE Trans. Geosci. Remote Sens., 51, 5225–5238, https://doi.org/10.1109/TGRS.2013.2272560, 2013.

Magnusson, M.: Near-wake behaviour of wind turbines, J. Wind Eng. Ind. Aerodyn., 80, 147–167, https://doi.org/10.1016/S0167-6105(98)00125-1, 1999.

Magnusson, M. and Smedman, A.-S.: Influence of Atmospheric Stability on Wind Turbine Wakes, Wind Engineering, 18, 139–152, 1994.

920   Maronga, B. et al.: Overview of the PALM model system 6.0, Geosci. Model Dev., 13, 1335–1372, https://doi.org/10.5194/gmd-13-1335-2020, 2020.

Martínez-Tossas, L. A., Churchfield, M. J., and Leonardi, S.: Large eddy simulations of the flow past wind turbines: Actuator line and disk modeling, Wind Energy, 18, 1047–1060, https://doi.org/10.1002/we.1747, 2015.

Martínez-Tossas, L. A., Churchfield, M. J., Yilmaz, A. E., Sarlak, H., Johnson, P. L., Sørensen, J. N., Meyers, J., and Meneveau, C.: Com-
925   parison of four large-eddy simulation research codes and effects of model coefficient and inflow turbulence in actuator-line-based wind turbine modeling, J. Renew. Sustain. Energy, 10, 033 301, https://doi.org/10.1063/1.5004710, 2018.

Mehta, D., van Zuijlen, A. H., Koren, B., Holierhoek, J. G., and Bijl, H.: Large Eddy Simulation of wind farm aerodynamics: A review, J. Wind Eng. Ind. Aerodyn., 133, 1–17, https://doi.org/10.1016/j.jweia.2014.07.002, 2014.

Meyers, J. and Meneveau, C.: Optimal turbine spacing in fully developed wind farm boundary layers, Wind Energy, 15, 305–317,
930   https://doi.org/10.1002/we.469, 2012.

Moens, M., Coudou, N., and Philippe, C.: A numerical study of correlations between wake meandering and loads within a wind farm, J. Phys. Conf. Ser., 1256, 012 012, https://doi.org/10.1088/1742-6596/1256/1/012012, 2019.

Moriarty, P., Rodrigo, J. S., Gancarski, P., Chuchfield, M., Naughton, J. W., Hansen, K. S., Machefaux, E., Maguire, E., Castellani, F., Terzi, L., Breton, S.-P., and Ueda, Y.: IEA-Task 31 WAKEBENCH: Towards a protocol for wind farm flow model evaluation. Part 2: Wind farm
935   wake models, J. Phys. Conf. Ser., 524, 012 185, https://doi.org/10.1088/1742-6596/524/1/012185, 2014.

Muller, Y.-A., Aubrun, S., and Masson, C.: Determination of real-time predictors of the wind turbine wake meandering, Exp. Fluids, 56, 53, https://doi.org/10.1007/s00348-015-1923-9, 2015.

Otsu, N.: A Threshold Selection Method from Gray-Level Histograms, IEEE Trans. Syst. Man. Cybern., 9, 62–66, https://doi.org/10.1109/TSMC.1979.4310076, 1979.

940   Porté-Agel, F., Wu, Y. T., Lu, H., and Conzemius, R. J.: Large-eddy simulation of atmospheric boundary layer flow through wind turbines and wind farms, J. Wind Eng. Ind. Aerodyn., 99, 154–168, https://doi.org/10.1016/j.jweia.2011.01.011, 2011.

Porté-Agel, F., Bastankhah, M., and Shamsoddin, S.: Wind-Turbine and Wind-Farm Flows: A Review, Boundary-Layer Meteorol., 174, 1–59, https://doi.org/10.1007/s10546-019-00473-0, 2020.

Pun, T.: Entropic thresholding, a new approach, Comput. Graph. Image Process., 16, 210–239, https://doi.org/10.1016/0146-664X(81)90038-1, 1981.

Quon, E. W., Doubrawa, P., and Debnath, M.: Comparison of Rotor Wake Identification and Characterization Methods for the Analysis of Wake Dynamics and Evolution, in: J. Phys. Conf. Ser., vol. 1452, p. 012070, Institute of Physics Publishing, https://doi.org/10.1088/1742-6596/1452/1/012070, 2020.

Shannon, C. E.: A Mathematical Theory of Communication, Bell Syst. Tech. J., 27, 379–423, https://doi.org/10.1002/j.1538-7305.1948.tb01338.x, 1948.

Snel, H., Schepers, J. G., and Montgomerie, B.: The MEXICO project (Model Experiments in Controlled Conditions): The database and first results of data processing and interpretation, in: J. Phys. Conf. Ser., vol. 75, p. 012014, IOP Publishing, https://doi.org/10.1088/1742-6596/75/1/012014, 2007.

Stevens, R. J.: Dependence of optimal wind turbine spacing on wind farm length, Wind Energy, 19, 651–663, https://doi.org/10.1002/we.1857, 2016.

Stevens, R. J. and Meneveau, C.: Flow Structure and Turbulence in Wind Farms, Annu. Rev. Fluid Mech., 49, 311–339, https://doi.org/10.1146/annurev-fluid-010816-060206, 2017.

Trujillo, J. J., Bingöl, F., Larsen, G. C., Mann, J., Kühn, M., Larsen, G. C., Trujillo, J. J., Bingöl, F., Larsen, G. C., Mann, J., Kühn, M., and Larsen, G. C.: Light detection and ranging measurements of wake dynamics part I: one-dimensional scanning, Wind Energy, 13, 51–61, https://doi.org/10.1002/we.352, 2010.

Trujillo, J.-J., Bingöl, F., Larsen, G. C., Mann, J., and Kühn, M.: Light detection and ranging measurements of wake dynamics. Part II: two-dimensional scanning, Wind Energy, 14, 61–75, https://doi.org/10.1002/we.402, 2011.

van der Laan, M. P. and Sørensen, N. N.: Why the Coriolis force turns a wind farm wake clockwise in the Northern Hemisphere, Wind Energy Sci., 2, 285–294, https://doi.org/10.5194/wes-2-285-2017, 2017.

Vollmer, L., van Dooren, M., Trabucchi, D., Schneemann, J., Steinfeld, G., Witha, B., Trujillo, J., and Kühn, M.: First comparison of LES of an offshore wind turbine wake with dual-Doppler lidar measurements in a German offshore wind farm, J. Phys. Conf. Ser., 625, 012 001, https://doi.org/10.1088/1742-6596/625/1/012001, 2015.

Vollmer, L., Steinfeld, G., Heinemann, D., and Kühn, M.: Estimating the wake deflection downstream of a wind turbine in different atmospheric stabilities: An LES study, Wind Energy Sci. Discuss., pp. 1–23, https://doi.org/10.5194/wes-2016-4, 2016.

Vollmer, L., Steinfeld, G., and Kühn, M.: Transient LES of an offshore wind turbine, Wind Energy Sci. Discuss., 2, 603–614, https://doi.org/10.5194/wes-2017-16, 2017.